ACCSCIENCE PUBLISHING

International Journal of Bioprinting

ACCEPTED PAPER · MAIN TEXT

Investigation of flowability and extrusion behavior of black soldier fly (*Hermetia illucens* L.) prepupal protein powder for 3D food printing applications

Article ID: IJB026250255

Citation: Oyinloye TM, Yongsawatdigul J, Chumee S, Hanboonsong Y, Yoon WB. Investigation of flowability and extrusion behavior of black soldier fly (*Hermetia illucens* L.) prepupal protein powder for 3D food printing applications. *Int J Bioprint*. 2026. doi: 10.36922/IJB026250255

AccScience Publishing
RESEARCH ARTICLE
Volume X Issue X (2026)
doi: 10.36922/IJB026250255

Investigation of flowability and extrusion behavior of black soldier fly (*Hermetia illucens* L.) prepupal protein powder for 3D food printing applications

Running title: Printability of black soldier fly paste

Timilehin Martins Oyinloye [1,2,3†], Jirawat Yongsawatdigul [4†], Sununta Chumee [4], Yupa Hanboonsong [5], and Won Byong Yoon [1,2,3*]

Name	ORCID
Timilehin Martins Oyinloye	https://orcid.org/0000-0003-3809-8982
Jirawat Yongsawatdigul	https://orcid.org/0000-0003-3778-5721
Won Byong Yoon	https://orcid.org/0000-0002-0370-8317

[1] Department of Food Science and Biotechnology, College of Agriculture and Life Sciences, Kangwon National University, Chuncheon 24341, Republic of Korea
[2] Elder-Friendly Food Research Center, Agriculture and Life Science Research Institute, Kangwon National University, Chuncheon 24341, Republic of Korea
[3] Department of Food Biotechnology and Environmental Science, Kangwon National University, Chuncheon 24341, Republic of Korea
[4] School of Food Technology, Institute of Agricultural Technology, Nakhon Ratchasima 30000, Thailand
[5] Department of Entomology, Faculty of Agriculture, Khon Kaen University, Khon Kaen 40002, Thailand

[†]*These authors contributed equally to this work.*

***Corresponding author:**
Won Byong Yoon (wbyoon@kangwon.ac.kr)

Citation: Oyinloye TM, Yongsawatdigul J, Chumee S, Hanboonsong Y, Yoon WB. Investigation of flowability and extrusion behavior of black soldier fly (*Hermetia illucens* L.) prepupal protein powder for 3D food printing applications. *Int J Bioprint.* 2026. doi: 10.36922/IJB026250255

Received: June 15, 2026
1st revised: July 16, 2026
2nd revised: July 21, 2026
Accepted: July 23, 2026
Published online: July 23, 2026

Abstract

Black soldier fly (*Hermetia illucens* L.) prepupae (BSFP) are a sustainable protein source, but the use of full-fat prepupal protein powder in extrusion-based three-dimensional food printing is limited by poor structure and flow control. This study developed black soldier fly prepupal protein-based pastes and evaluated the effects of tapioca starch concentration and thermal treatment on rheology, die swell, and printing stability. Pastes were formulated at 80% moisture content using 0.5% gellan gum, tapioca starch at 0, 2.5, or 5%, and corresponding BSFP powder contents of 24.87, 21.98, and 19.09%, respectively. Thermal treatment significantly strengthened the paste structure, increasing the initial storage modulus to 3998.56, 6248.78, and 8891.23 Pa for 0%, 2.5%, and 5% starch, respectively. Steady shear analysis showed shear-thinning behavior, while model-estimated yield stress after heating increased from 363.58 to 636.06 Pa with starch addition. Large-amplitude oscillatory shear and Chebyshev coefficient analysis showed that starch increased nonlinear elastic resistance and strain stiffening. However, 5% starch caused the high die swell ratio of 1.96 and edge roughness of 0.074 mm. The 2.5% starch formulation showed the lowest edge roughness of 0.049 mm and thickness variation of 8.1%, producing the most stable printed structure. Overall, moderate starch addition improved printability by balancing flow, recovery, and shape retention.

Keywords: Black soldier fly prepupae powder; Small-amplitude oscillatory shear; Large-amplitude oscillatory shear; Die swell; 3D printing; Image analysis

1. Introduction

Black soldier fly prepupae (BSFP; *Hermetia illucens* L.) have attracted interest as a sustainable protein source because they can convert low-value organic side streams into nutrient-rich biomass with rapid growth and short production cycles.[1,2] Their composition varies with feeding substrate, developmental stage, and processing conditions, but black soldier fly larvae and prepupae commonly contain substantial protein and lipid fractions and provide essential amino acids.[1–3] These characteristics support their potential use in protein-enriched and structured foods. However, successful incorporation into such products depends not only on nutritional composition but also on hydration, flow behavior, deformation resistance, and structural stability during processing.

Full-fat BSFP powder differs from purified protein isolates or concentrates because it contains protein together with lipid, carbohydrate, minerals, chitin-containing fractions, and insoluble particles.[2,4] This heterogeneous composition can influence water binding, particle interactions, lubrication, viscosity, and paste cohesion. Such properties are particularly important in direct ink writing, where a material must pass through a narrow nozzle while maintaining sufficient strength after deposition.[5] Therefore, the printing behavior of full-fat BSFP powder cannot be assumed to be identical to that of conventional purified protein inks.

Direct ink writing (3-dimensional printing) is an extrusion-based additive-manufacturing process in which a viscoelastic material is deposited layer by layer according to a predefined digital design.[5–8] A suitable food ink should flow continuously under the shear and pressure generated inside the nozzle, but it should rapidly recover enough structure after extrusion to prevent spreading, deformation, and collapse. If the material is too fluid, the deposited layers lose their intended geometry; if it is excessively stiff or elastic, extrusion may become unstable, and nozzle blockage, irregular deposition, or excessive die swell may occur. Consequently, printability depends on a balance among viscosity, yield behavior, shear thinning, viscoelasticity, structural recovery, and dimensional stability.[7–9]

Hydrocolloids and starches are widely used in 3D food printing to improve these properties. Hydrocolloids such as xanthan gum, guar gum, carrageenan, alginate, and gellan gum have been used to modify food-ink rheology and improve printability.[10,11] Starches can also increase paste

body, support gel formation, and improve the mechanical stability of printed structures.[12–15] Their combined use may help convert a weak particulate suspension into a printable structured paste. However, excessive reinforcement may also increase elastic recovery after nozzle exit, leading to filament expansion, surface roughness, and dimensional errors. The optimal formulation is therefore not necessarily the formulation with the highest modulus or viscosity.

Thermal treatment is also important in BSFP-based food systems. Heating can improve microbiological safety while simultaneously modifying protein structure, starch gelatinization, and hydrocolloid network formation.[16,17] Protein unfolding and aggregation may increase structural strength, whereas starch swelling and gellan-chain association may further reinforce the continuous phase.[18,19] These transformations can improve post-deposition shape retention, but they may also increase extrusion resistance and elastic recoil. Understanding the combined effects of formulation and thermal treatment is therefore necessary for developing BSFP-based inks with controlled flow and stable printing performance.

Rheological analysis is needed to understand these formulations and processing effects. Small-amplitude oscillatory shear (SAOS) is commonly used to characterize linear viscoelastic behavior, including storage modulus, loss modulus, and the linear viscoelastic region.[20] These measurements describe the weakly deformed structure. However, 3D printing exposes materials to large deformation during nozzle flow, and linear measurements alone may not fully represent their response during extrusion.

Large-amplitude oscillatory shear (LAOS) analysis provides additional information on nonlinear deformation, structural breakdown, strain stiffening, strain softening, and intra-cycle shear thinning.[20] Chebyshev coefficients can separate elastic and viscous nonlinear contributions and help explain how a paste resists deformation inside the nozzle and recovers after deposition.[6] These measurements are particularly relevant when a formulation shows high elasticity, because stored elastic energy can be released after nozzle exit and produce die swell or dimensional distortion.

Although many protein-based materials have been investigated for 3D food printing, most studies have focused on conventional or purified protein systems and have evaluated printability mainly through viscosity, linear viscoelasticity, and qualitative images. Limited information is

available on the behavior of full-fat insect-derived powders as heterogeneous particulate matrices. In particular, the relationships among BSFP powder properties, thermal treatment, nonlinear rheology, die swell, filament uniformity, dimensional fidelity, and post-print stability remain unclear.

Recent work has also emphasized the need to replace subjective trial-and-error evaluation with quantitative and data-driven approaches. Zhang et al.[21] proposed an end-to-end artificial-intelligence framework for evaluating and optimizing direct ink writing using material, processing, and printing-quality data. Their study demonstrates that reliable optimization requires objective descriptors of both material behavior and printed geometry. Although AI-based optimization was beyond the scope of the present work, the same principle supports the use of quantitative rheological and printing-quality measurements when evaluating new food inks. The novelty of this study, therefore, lies in establishing an integrated material–rheology–extrusion–printing relationship for a multicomponent full-fat BSFP powder. Powder water solubility and particle-size distribution were combined with small-amplitude oscillatory shear, steady shear, large-amplitude oscillatory shear, Chebyshev analysis, die-swell measurement, filament-uniformity analysis, quantitative shape fidelity, and post-print structural stability. This approach was used to determine whether increasing starch-induced structural strength necessarily improves printing performance and to identify the formulation that best balances nozzle flow, elastic recovery, dimensional accuracy, and shape retention.

Therefore, this study aimed to develop full-fat BSFP powder-based pastes for direct ink writing and evaluate the effects of tapioca starch concentration and thermal treatment on their rheological and printing behavior. The specific objectives were to: (i) characterize the composition, hydration properties, water solubility, and particle-size distribution of the BSFP powder; (ii) determine the effects of starch addition and thermal treatment on linear, steady-shear, and nonlinear viscoelastic properties; (iii) relate nonlinear deformation and elastic recovery to die swell and filament quality; and (iv) quantitatively evaluate the dimensional fidelity and post-print structural stability of the printed structures.

2. Materials and methods

2.1 Sample preparation

Black soldier fly prepupae (BSFP) reared on expired fruits and vegetables were obtained according to the rearing protocol described by Katemala *et al.*[2] Prepupae were harvested at the prepupal stage (20-25 days old) from the Pilot Greenhouse for Industrial Insect Research and Production, Industrial Insect Division, Khon Kaen University, Thailand. The harvested insects were cleaned to remove residual substrate and stored at −18 °C for 3 days before transportation to Suranaree University of Technology, Thailand, for further processing. Frozen samples were thawed at 4 °C for 16-24 h and subsequently blanched in boiling water (100-105 °C) using a sample-to-water ratio of 1:10 (w/v) for 1 min to inactivate endogenous enzymes and reduce microbial load. Immediately after blanching, the samples were cooled in an ice-water bath, and excess surface water was removed by blotting dry. The samples were then dried using a tray dryer at 70 °C for 6 h. Dried prepupae were ground into a fine, full-fat BSFP powder using a grinder (Philips Blender 3000 Series, Philips, China).

Modified tapioca starch (TS; acetylated distarch phosphate; INS 1414) obtained from Siam Quality Starch Co., Ltd. (Nakhon Ratchasima, Thailand), was used as a structuring material to improve paste consistency, elastic recovery, and shape stability during printing. Gellan gum (GG; mid-low acyl, manufactured by Xinjiang Fufeng Biotechnologies Co., Ltd., China, and distributed by T.C.S Pacific, Thailand) was used as a hydrocolloid to improve water binding and support gel-like network formation in the BSFP paste.

Preliminary rheological screening was first conducted to identify suitable base levels of BSFP powder and gellan gum. Based on the screening results presented in Figure S1 and Table S1, 7.5% BSFP powder and 0.5% GG were selected as the initial screening conditions. For the final formulations, GG was maintained at 0.5%, while TS was incorporated at 0, 2.5, and 5%. The amounts of BSFP powder and distilled water were adjusted, as shown in Table 1, to maintain approximately 80% total moisture to obtain a paste suitable for extrusion-based 3D printing. After mixing, the samples were homogenized for 16 h to allow complete hydration of the BSFP powder and uniform dispersion of the dry ingredients.

Table 1. Nominal formulation of BSFP-based pastes.

	Material composition		
Sample code	**BG-S0**	**BG-S2.5**	**BG-S5**
Distilled water (ml)	74.63	75.02	75.41
BSFP-powder (g)	24.87	21.98	19.09
Tapioca starch (g)	0	2.50	5.00
Gellan gum (g)	0.50	0.50	0.50
Total	100.0	100.0	100.0

BG-S0, BG-S2.5, and BG-S5 represent the final formulations containing 0, 2.5, and 5% tapioca starch, respectively. BG denotes the BSFP-gellan gum formulation, while S indicates the tapioca starch level.

2.2 Characterization of BSFP Powder

2.2.1 Proximate Composition Analysis

The proximate composition of BSFP samples was analyzed according to the official methods of the Association of Official Analytical Chemists[22]. Moisture, crude protein, and ash contents were determined following AOAC methods 934.01, 976.05, and 942.05, respectively. Moisture content was measured by oven drying at 105 °C until constant weight was achieved. Crude protein content was determined using the Kjeldahl method with a nitrogen-to-protein conversion factor of 6.25. Total lipid content was analyzed using the method of Folch *et al.*[23], in which samples were homogenized in a chloroform–methanol mixture (2:1, v/v), followed by phase separation and recovery of the lipid-containing organic phase. Ash content was determined by incineration in a muffle furnace at 550 °C. Carbohydrate content was calculated by difference as follows:

$$\text{Carbohydrate (\%)} = 100 - [\text{moisture (\%)} + \text{crude protein (\%)} + \text{lipid (\%)} + \text{ash (\%)}] \quad \text{(I)}$$

All values were expressed on a wet weight basis.

2.2.2 Water Absorption or Hydration Behavior

Water-holding capacity (WHC) was determined following the method of Mshayisa *et al.*[24] with slight modifications. Briefly, 0.1 g of protein powder was mixed with 1 mL of deionized water and vortex-mixed for 1 min using a Vortex-Genie 2 mixer (Scientific Industries Inc., Bohemia, NY, USA). The suspension was then centrifuged at 4,000 × g for 5 min at 4 °C to separate unbound water. After centrifugation, the supernatant was discarded, loosely bound water was carefully removed, and the weight of the hydrated sample was recorded. WHC was expressed as the percentage increase in sample weight after water absorption.

Oil-holding capacity (OHC) was determined using the same procedure, except that commercial soybean oil was used instead of deionized water, and the mixture was vortex-mixed for 2 min before centrifugation. Following centrifugation, loosely bound oil was removed before weighing. OHC was calculated using the same equation used for WHC. All measurements were conducted in triplicate. Absorption capacity (%) was calculated using the following Equation II:

$$\text{Absorption (\%)} = \frac{\text{Final weight} - \text{Initial weight}}{\text{Initial weight}} \times 100 \qquad \text{(II)}$$

2.2.3 Water solubility of BSFP powder

The water solubility was determined using a centrifugation–gravimetric method adapted from Mshayisa *et al.*[24] Briefly, 0.5 g of BSFP powder was dispersed in 25 mL of deionized water to obtain a 2% (w/v) suspension. The suspension was continuously stirred at room temperature for 60 min to allow hydration and extraction of the water-soluble components. After mixing, the suspension was centrifuged at 4000 × g for 20 min at 4 °C to separate the water-soluble fraction from the insoluble material. The supernatant was carefully collected without disturbing the sediment. A known volume of the supernatant was transferred into a pre-weighed drying dish and dried in an oven at 105 °C until a constant weight was obtained. The mass of water-soluble solids in the complete supernatant was calculated from the dry residue obtained from the measured aliquot. Water solubility was calculated using Equation (III):

$$\text{Water solubility (\%)} = \frac{m_s \times V_t}{V_a \times m_0} \times 100 \qquad \text{(III)}$$

where m_s is the mass of dried soluble solids obtained from the supernatant aliquot, V_t is the total volume of the collected supernatant, V_a is the volume of the supernatant aliquot used for drying, and m_0 is the initial dry mass of BSFP powder. All measurements were conducted in triplicate, and the results were expressed as mean ± standard deviation.

2.2.4 Particle-size distribution of BSFP powder

The particle-size distribution of the full-fat BSFP powder was determined by dry mechanical sieving according to the general principles of ISO 2591-1, with slight modifications.[25] The test sieves were arranged in descending order of nominal aperture size as follows: 1400, 1180, 1000, 600, 425, 250, and 150 µm. A receiving pan was placed below the 150 µm sieve to collect particles smaller than 150 µm. Accordingly, the powder was separated into eight particle-size fractions: >1400, 1180–1400, 1000–1180, 600–1000, 425–600, 250–425, 150–250, and <150 µm.

Before analysis, the BSFP powder was equilibrated to room temperature in a sealed container. A representative 100 g portion of powder was weighed and placed on the uppermost 1400 µm sieve. The sieve stack was covered and mounted on a mechanical sieve shaker (CG-211-8, Chunggye, Seoul, South Korea). The sample was sieved for 10 min at a constant shaker setting. After sieving, the material retained on each sieve and in the receiving pan was carefully collected and weighed using an analytical balance. The percentage of powder retained in each particle-size fraction was calculated using Equation (IV):

$$R_i\ (\%) = \frac{m_i}{m_0} \times 100 \qquad \text{(IV)}$$

where R_i is the percentage of powder retained on sieve i, m_i is the mass of powder retained on that sieve, and m_0 is the initial mass of powder subjected to sieving. A mass recovery between 98 and 100% was considered acceptable. The analysis was conducted in triplicate using independently weighed powder portions, and the percentage retained in each size fraction was expressed as mean ± standard deviation.

Cumulative percentage passing was calculated from the retained mass data and used to determine D_{10}, D_{50}, and D_{90}, representing the particle diameters below which 10%, 50%, and 90% of the powder mass were distributed, respectively. Because these target percentages generally

occurred between two adjacent sieve apertures, the corresponding particle diameters were estimated by logarithmic interpolation. The distribution span was calculated as $(D_{90}-D_{10})/D_{50}$ to describe the breadth of the particle-size distribution. Normal and Weibull probability-density models were fitted to the experimental sieve distribution. For the normal model, the mean particle size and standard deviation were calculated from the probability-weighted representative particle sizes. For the Weibull model, the cumulative passing fraction, F(x), was linearized as $\ln\left[-\ln\left(1-\mathrm{F(x)}\right)\right] = \mathrm{k}\ln(\mathrm{x}) - \mathrm{k}\ln(\lambda)$. The shape parameter k was obtained from the slope of the linear regression, while the scale parameter λ was calculated from the intercept as $\lambda = \exp(-\mathrm{b}/\mathrm{k})$, where b is the regression intercept. The resulting Weibull parameters were k = 1.94 and λ = 673.9 μm. Model performance was evaluated using the sum of squared errors (SSE) and root mean squared error (RMSE) between observed and predicted bin probabilities, with lower values indicating a better fit.

2.3 Thermal treatment of BSFP-based paste

Thermal treatment was conducted to evaluate the effect of heating on the rheological and printing behavior of the BSFP-based paste. The prepared paste was transferred into conical tubes and heated in a water bath (WCB-11, DAIHAN Scientific Co., Ltd., Wonju, Republic of Korea) at 90 °C for 30 min. After heating, the samples were cooled to room temperature before rheological and printing analyses. The untreated samples were analyzed without heating and were used to evaluate the original paste behavior before thermal processing.

2.4 Small Amplitude Oscillatory Shear measurement of BSFP-based paste

The rheological properties of the BSFP-based paste were measured using a Discovery Hybrid Rheometer HR-3 (TA Instruments, New Castle, DE, USA). A 40 mm parallel plate geometry with a Peltier temperature control system was used. The gap between the upper plate and the Peltier plate was maintained at 1.0 mm. The measurement temperature was set at 25 °C to evaluate the paste under room-temperature printing conditions. The sample was allowed to rest for

5 min before measurement to reduce the effect of loading stress. A solvent trap was used to minimize moisture loss during measurement.

Small-amplitude oscillatory shear (SAOS) tests were conducted to evaluate the linear viscoelastic behavior of the BSFP-based paste before and after thermal treatment. A strain sweep was first performed from 0.01 to 100% strain at a constant angular frequency of 1 rad/s. This test was used to determine the linear viscoelastic region (LVR). The LVR was identified as the strain range where the storage modulus (G') and loss modulus (G") remained nearly constant with increasing strain. A frequency sweep was then conducted from 0.1 to 100 rad/s at a fixed strain within the LVR. The G' and G" were recorded to compare the elastic and viscous characteristics of the formulations.

Steady shear measurements were conducted to evaluate flow behavior under extrusion-relevant deformation. The shear rate was increased from 0.1 to 100 s^{-1}, and the corresponding shear stress and apparent viscosity were recorded. The Herschel–Bulkley model was used to describe the flow behavior.[26]

$$\tau = \tau_0 + K\dot{\gamma}^n \qquad (V)$$

where τ is the shear stress (Pa), τ_0 is the yield stress (Pa), K is the consistency coefficient ($Pa \cdot s^n$), $\dot{\gamma}$ is the shear rate (s^{-1}), and n is the flow behavior index. The Herschel–Bulkley parameters were used to compare yield behavior, flow resistance, and shear-thinning characteristics among the BSFP-based formulations. A value of ($n < 1$) indicates shear-thinning behavior, which is important for extrusion-based 3D printing because it allows the paste to flow more easily under nozzle shear.

For the untreated BSFP-based paste, a temperature sweep was also conducted to evaluate heat-induced structural development. The sample was heated from 25 to 100 °C at a heating rate of 5 °C/min. Changes in G' and G" during heating were recorded to determine how the paste structure developed as the temperature increased. This test was used to support the interpretation of structural changes that may occur during thermal processing.

2.5 Large Amplitude Oscillatory Shear measurement of BSFP-based paste

Large-amplitude oscillatory shear (LAOS) measurements were conducted to evaluate the nonlinear deformation behavior of the BSFP-based paste under large deformation. The analysis was performed using a Discovery Hybrid Rheometer HR-3 (TA Instruments, New Castle, DE, USA) equipped with a 40 mm parallel plate geometry and a Peltier temperature control system. The measurement gap was maintained at 1.0 mm, and the test temperature was set at 25 °C. LAOS tests were performed at a constant angular frequency of 1 rad/s. The strain amplitude was increased from 0.5 to 1000% to evaluate the transition from small deformation to large nonlinear deformation. The raw stress, strain, and shear-rate waveforms were collected from the rheometer software at each strain amplitude. These raw data were used to construct Lissajous curves in stress–strain and stress–shear rate coordinates. The curves were used to compare deformation resistance, structural breakdown, and nonlinear flow behavior among the BSFP-based formulations.

The nonlinear viscoelastic response was analyzed from the raw waveform data exported from the rheometer software and processed in MATLAB R2025b (MathWorks, Natick, MA, USA) using a freely available LAOS data analysis package, MITlaos software (MITlaos beta).[27] The software was used to obtain Fourier coefficients, Chebyshev coefficients, elastic and viscous stress decomposition, and nonlinear viscoelastic parameters. For each LAOS condition defined by angular frequency (ω) and strain amplitude (γ_0), the sample was subjected to repeated deformation cycles until a steady-state limit cycle was reached.

The elastic Chebyshev coefficients were expressed as e_1, e_3, e_5, and higher odd harmonics. The viscous Chebyshev coefficients were expressed as v_1, v_3, v_5, and higher odd harmonics. The ratios e_3/e_1 and v_3/v_1 were used to describe the nonlinear elastic and viscous contributions, respectively. In the linear viscoelastic region, the contribution of higher harmonics is very small, and e_3 and v_3 approach zero.[27] A positive e_3/e_1 value indicates intra-cycle strain stiffening, while a negative e_3/e_1 value indicates strain softening. Similarly, a positive v_3/v_1 value indicates intra-cycle shear thickening, while a negative v_3/v_1 value indicates intra-cycle shear thinning.

The minimum-strain modulus and large-strain modulus were calculated from the elastic Chebyshev coefficients using Equations (VI) and (VII)[28]:

$$G'_M = \left.\frac{d\sigma}{d\gamma}\right|_{\gamma=0} \approx e_1 - 3e_3 + 5e_5 - 7e_7 + \cdots \qquad (VI)$$

$$G'_L = \left.\frac{\sigma}{\gamma}\right|_{\gamma=\pm\gamma_0} \approx e_1 + e_3 + e_5 + e_7 + \cdots \qquad (VII)$$

where G'_M represents the minimum-strain modulus, and G'_L is the large-strain modulus. These parameters describe the elastic response of the paste within each oscillation cycle.

The minimum-rate and large-rate dynamic viscosities were calculated from the viscous Chebyshev coefficients using Equations (VIII) and (IX)[28]:

$$\eta'_M = \left.\frac{d\sigma}{d\dot{\gamma}}\right|_{\dot{\gamma}=0} \approx v_1 - 3v_3 + 5v_5 - 7v_7 + \cdots \qquad (VIII)$$

$$\eta'_L = \left.\frac{\sigma}{\dot{\gamma}}\right|_{\dot{\gamma}=\pm\dot{\gamma}_0} \approx v_1 + v_3 + v_5 + v_7 + \cdots \qquad (IX)$$

where η'_M is the minimum-rate dynamic viscosity, and η'_L is the large-rate dynamic viscosity. These values describe the viscous response of the paste during each oscillation cycle.

The strain stiffening ratio (S) and shear thickening ratio (T) were calculated using Equations (X) and (XI)[28]:

$$S = \frac{G'_L - G'_M}{G'_L} \approx \frac{4e_3 - 4e_5 + 8e_7 + \cdots}{e_1 + e_3 + e_5 + e_7 + \cdots} \qquad (X)$$

$$T = \frac{\eta'_L - \eta'_M}{\eta'_L} \approx \frac{4v_3 - 4v_5 + 8v_7 + \cdots}{v_1 + v_3 + v_5 + v_7 + \cdots} \qquad (XI)$$

Positive S values indicate intra-cycle strain stiffening, while negative S values indicate strain softening. Positive T values indicate intra-cycle shear thickening, while negative T values indicate intra-cycle shear thinning. These nonlinear parameters were used to explain how formulation affected structural breakdown, elastic recovery, and flow behavior under the large deformation conditions relevant to nozzle extrusion.[29]

2.6 Direct ink writing and quantitative printing-quality evaluation of BSFP-based pastes

2.6.1 3D printing process and model design

The extrusion and printing behavior of the BSFP-based paste was evaluated using an extrusion-based direct ink writing printer (SHINNOVE-S2, Shinnove Co. Ltd., Hangzhou, Zhejiang, China). The prepared paste was loaded into a printer syringe and extruded through a 1.2 mm nozzle at a printing speed of 1 mm/s under controlled room-temperature conditions. An open-ended cubic model with dimensions of 20 mm × 20 mm × 20 mm and a nominal wall thickness of 2.4 mm was printed to evaluate continuous extrusion, filament deposition, layer stacking, dimensional fidelity, and post-printing structural stability (Figure 1a). The open-box geometry was selected because its vertical walls and unsupported internal space allowed changes in spreading, wall deformation, layer collapse, and shape retention to be clearly observed.

Images were captured under fixed camera position, lighting, and background conditions at 5, 30, 60, 90, 120, and 150 s during printing. An additional image was captured 10 min after completion of printing to evaluate post-deposition structural stability. The camera distance and image resolution were kept constant for all samples. A scale reference was included within the image field for pixel-to-millimeter calibration.

To evaluate extrusion behavior independently of the complete three-dimensional structure, a straight filament with a target length of 50 mm was printed using the same 1.2 mm nozzle and printing conditions (Figure 1b). The straight filament was used to determine die swell, edge roughness, and thickness uniformity.

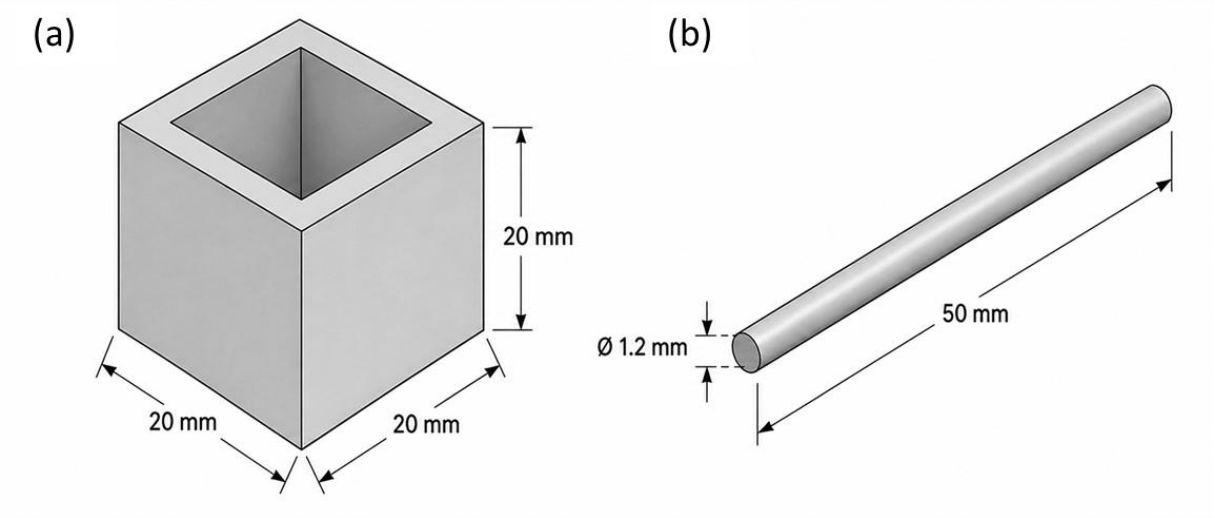

Figure 1. Schematic representation of the models used for BSFP paste printing evaluation: (a) open-ended cubic model and (b) straight-line filament model for die swell analysis.

2.6.2 Image acquisition and die swell analysis

Images of the printed filaments were captured using a digital camera (DSLR-500D, Canon Inc., Tokyo, Japan) under fixed imaging conditions. The camera position (200 mm away from the extrudate), lighting, and background were kept constant during image acquisition to minimize measurement variation. A black background was used to improve contrast between the extruded paste and the surrounding area. The image resolution and camera distance were recorded for pixel-to-millimeter calibration. The final calibration factor was 12.853 pixels/mm.

Image analysis was performed using MATLAB R2025b (MathWorks, Natick, MA, USA). The captured RGB images were first converted to grayscale. The filament was then separated from the background using image thresholding. The segmented image was converted into a binary image, and small isolated regions were removed before analysis.

The left and right filament boundaries were detected along the printing direction (Figure 2). Local filament width was calculated at each image row as the distance between the two boundaries and converted from pixels to millimeters using the calibration factor. The mean filament width was used to calculate the die-swell ratio using Equation (XII):

$$Die\ swell\ ratio = \frac{W_f}{W_D} \qquad \text{(XII)}$$

where W_f is the mean printed filament width, and W_D is the nozzle diameter.

Edge roughness was determined from the deviation of the detected filament boundaries from fitted reference lines. The absolute deviations of the left and right boundaries were averaged and converted to millimeters. A lower value indicated a smoother and more uniform extruded filament.

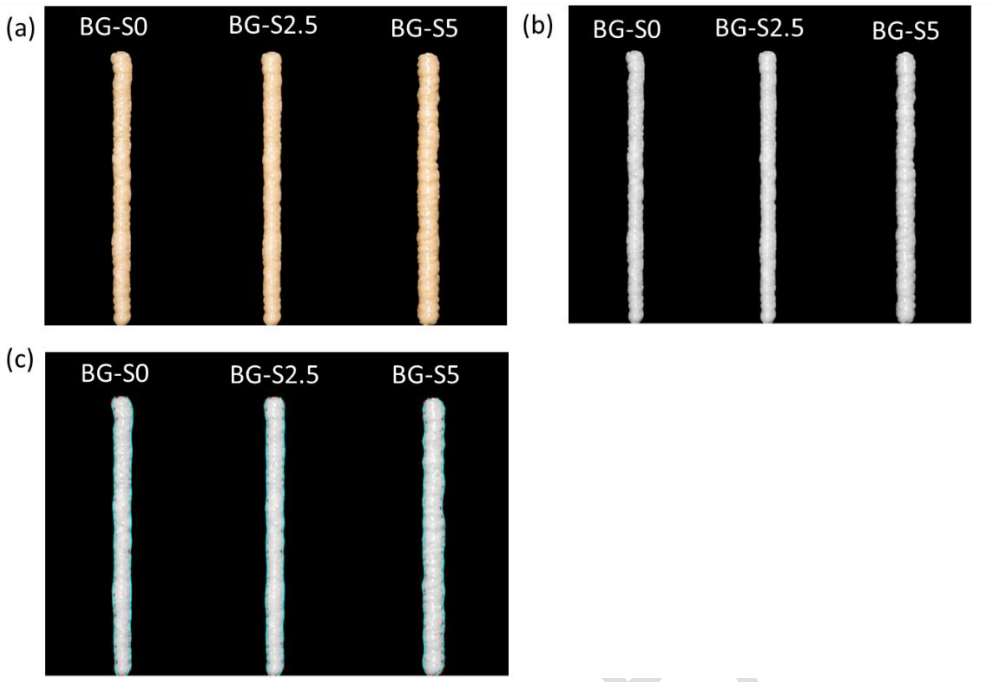

Figure 2. Image-processing steps used for printed BSFP-based filaments: (a) original RGB images, (b) grayscale conversion, and (c) edge/boundary detection for filament thickness analysis.

2.6.3 Quantitative shape-fidelity analysis of the open-box structures

The images of the open-box structures were quantitatively analyzed using MATLAB R2025b. The printed structure was segmented from the background, and its outer boundaries were identified. The final printed height, external width, and apparent wall thickness were measured after completion of printing. Printed height was determined as the vertical distance between the printing surface and the highest point of the structure. External width was measured between the outermost left and right boundaries. Wall thickness was measured at several evenly spaced positions along the vertical walls, and the mean value was calculated.

Height fidelity was calculated by comparing the measured printed height with the designed height using Equation (XIII):

$$Height\ fidelity\ (\%) = \frac{H_p}{H_D} \times 100 \qquad \text{(XIII)}$$

where H_p is the measured printed height and H_d is the designed height of 20 mm.

Width accuracy was calculated using Equation (XIV):

$$Width\ accuracy\ (\%) = \left(1 - \frac{|W_p - W_D|}{W_D}\right) \times 100 \qquad \text{(XIV)}$$

where W_p is the measured external width of the printed structure and W_D is the designed width of 20 mm.

Wall-thickness accuracy was calculated using Equation (XV):

$$Wall - thickness\ accuracy\ (\%) = \left(1 - \frac{|T_p - T_D|}{T_D}\right) \times 100 \qquad \text{(XV)}$$

where T_p is the mean measured wall thickness and T_D is the designed wall thickness of 2.4 mm.

An overall dimensional fidelity index was calculated as the average of the height, width, and wall-thickness accuracy values:

$$Overall\ shape\ fidelity\ (\%) = \frac{Height\ fidelity + Width\ accuracy + Wall - thickness\ accuracy}{3} \qquad \text{(XVI)}$$

Higher values indicated closer agreement between the printed structure and the designed model.

The post-printing structural stability was evaluated by comparing the dimensions of each open-box structure immediately after printing and 10 min after printing. The height and external width of the structure were measured from the calibrated images at both time points.

Height retention was calculated using Equation (XVII):

$$Height\ retention\ (\%) = \frac{H_{10}}{H_0} \times 100 \qquad \text{(XVII)}$$

where H_0 is the structure height immediately after printing and H_{10} is the height measured 10 min after printing. Post-print spreading was calculated using Equation (XVIII):

$$Spreading\ (\%) = \frac{W_{10} - W_0}{W_0} \times 100 \qquad \text{(XVIII)}$$

where W_0 is the external width immediately after printing and W_{10} is the width measured 10 min after printing.

Structural deformation was calculated from the combined changes in height and width:

$$Structural\ deformation\ (\%) = \frac{\left|\frac{H_{10} - H_0}{H_0}\right| + \left|\frac{W_{10} - W_0}{W_0}\right|}{2} \times 100 \qquad \text{(XIX)}$$

A higher height-retention value and lower spreading and deformation values indicated better post-printing structural stability. Three independently printed structures were evaluated for each formulation.

2.7 Scanning electron microscopy

The surface microstructures of the BSFP powder and thermally treated BG-S0, BG-S2.5, and BG-S5 formulations were examined using scanning electron microscopy. The thermally treated BG-S0, BG-S2.5, and BG-S5 samples were freeze-dried before SEM analysis, while the original BSFP powder was examined in its dry powdered form. The dried samples were fractured into small pieces and mounted on aluminium specimen stubs using double-sided conductive carbon tape. The mounted samples were coated with a thin layer of gold using a sputter coater to minimize surface charging. Micrographs were obtained using a scanning electron microscope (Model SU8600, Hitachi High-Tech Corporation, Tokyo, Japan) operated at an accelerating voltage of 5.0 kV and a working distance of approximately 10 mm. Images were collected at magnifications of ×300 to compare the overall structure, particle–matrix organization, surface continuity, aggregation, pores, and structural heterogeneity of the formulations.

2.8 Texture profile analysis of printed structures

The textural properties of the printed BG-S2.5, BG-S5, and TS-only samples were evaluated using a texture analyzer (Stable Micro Systems, Surrey, UK). Samples with identical printed dimensions were allowed to rest at room temperature for 10 min and subjected to a two-cycle compression test using a cylindrical probe (Diameter, 30 mm). Each sample was compressed to 50% of its original height at a test speed of 1 mm/s, with a 5 s interval between compression cycles. Hardness, adhesiveness, springiness, cohesiveness, gumminess, chewiness, and resilience

were obtained directly from the instrument software. Five independently printed samples were analyzed for each formulation, and the results were expressed as mean ± standard deviation.

2.9 Statistical analysis

All experiments were conducted using independently prepared samples. Powder characterization and printing-quality measurements were performed in triplicate, while texture profile analysis was conducted using five independently printed samples per formulation. Data were expressed as mean ± standard deviation. Statistical analysis was performed using SPSS Statistics version 19.0. Differences among formulations were evaluated by one-way analysis of variance followed by Duncan's multiple range test. Differences were considered statistically significant at $p < 0.05$.

3.0 Results and discussion

3.1 Proximate composition, functional properties, and particle-size characteristics of full-fat BSFP powder

The proximate composition, functional properties, and particle-size characteristics of the full-fat BSFP powder are presented in Table 2. The powder contained 28.49% protein and 24.05% lipid, confirming that it was a protein-rich but compositionally complex ingredient rather than a purified protein concentrate. The relatively high lipid content may influence lubrication, water–solid interactions, flow resistance, and filament formation during extrusion. The carbohydrate fraction may also include structural components such as chitin, which can contribute to water binding, particle interactions, and paste consistency. Similar compositional complexity has been reported for black soldier fly-derived flours and protein materials, whose functional behavior depends strongly on the proportions of protein, lipid, fiber, and other non-protein components.[24,30]

The BSFP powder showed a water-holding capacity of 135.33% and an oil-holding capacity of 74.23%, indicating its ability to retain both aqueous and lipid phases within the paste matrix. Sufficient water retention is important for the hydration of BSFP particles, tapioca starch, and gellan gum, whereas oil retention and the naturally high lipid content may modify interparticle

lubrication and flow behavior. BSFP proteins have also been reported to possess gel-forming potential, although their network development is strongly affected by processing conditions, protein aggregation, hydrophobic interactions, and non-protein components.[30]

The water solubility of the powder was 20.11 ± 1.29%, showing that only a limited proportion of the dry matter entered the aqueous phase, while most remained as dispersed or sedimentable particles. This limited solubility is consistent with the full-fat and minimally refined nature of the material, which contains insoluble proteins, lipid-associated particles, chitin, and other structural fractions. The insoluble fraction may increase interparticle contact, paste viscosity, and resistance during nozzle flow.

The particle-size distribution is shown in Figure 3. The dominant fraction was 600–1000 µm, accounting for approximately 42% of the powder, followed by the 425–600 and 250–425 µm fractions at approximately 20% and 18%, respectively. The calculated D_{10}, D_{50}, and D_{90} values were 220.38, 600.00, and 975.97 µm, respectively, with a distribution span of 1.26, confirming a broad and heterogeneous particle-size distribution. Normal and Weibull distributions were fitted to the sieve data, and the predicted mass percentages within each sieve fraction were compared with the observed values. The normal distribution provided the closer fit, with an RMSE of 0.0170 and an SSE of 0.0023. In comparison, the Weibull model showed an RMSE of 0.0634 and an SSE of 0.0322. Although both models reproduced the major distribution peak, the lower fitting errors of the normal model indicate that it described the observed sieve-bin probabilities more accurately. Finer particles may hydrate more rapidly and improve matrix continuity, whereas larger particles may increase interparticle friction, extrusion resistance, filament roughness, and dimensional variation. Therefore, the printing behavior of the formulations likely resulted from the combined effects of dispersed BSFP particles and the continuous starch–gellan network. Overall, the composition, limited solubility, hydration capacity, and broad particle-size distribution demonstrate the need for additional structuring ingredients to improve cohesion, flow control, and post-deposition stability for BSFP powder.

Table 2. Proximate composition, functional properties, water solubility, and particle-size characteristics of full-fat BSFP powder.

Proximate composition (%)	
Moisture	21.38 ± 0.44
Protein	28.49 ± 1.16
Fat	24.05 ± 1.24
Ash	1.36 ± 0.02
Carbohydrate*	24.72
Functional properties	
Water-Holding Capacity (WHC, %)	135.33 ± 3.37
Oil-Holding Capacity (OHC, %)	74.23 ± 5.37
Water solubility (%)	20.11 ± 1.29
Particle-size characteristics	
D_{10} (μm)	220.38
D_{50} (μm)	600.00
D_{90} (μm)	975.97
Span, $(D_{90}-D_{10})/D_{50}$	1.26

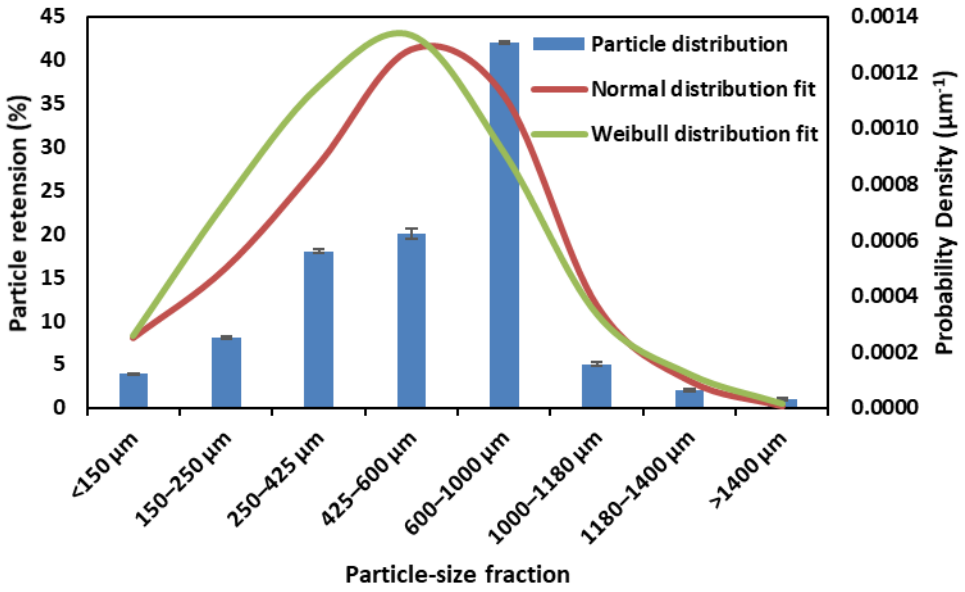

Figure 3. Particle-size distribution of full-fat BSFP powder. Bars represent the mean mass percentage retained within each sieve fraction, and error bars indicate the standard deviation of three independent measurements. Solid lines represent the retained mass percentages predicted by the normal and Weibull distribution models.

3.2 Rheological properties of BSFP-based paste

3.2.1 Linear viscoelastic behavior of BSFP-based paste before and after thermal treatment

The linear viscoelastic properties of BSFP-based paste before and after thermal treatment are shown in Figure 4. Before thermal treatment, all BSFP-based pastes showed elastic-dominant behavior within the low-strain region. For the 0% starch sample, G' remained higher than G" up to approximately 2.91% strain, while the 2.5% and 5% starch samples maintained G'>G" up to 6.93% and 8.89% strain, respectively, indicating better resistance to deformation with starch addition.

After thermal treatment, the modulus increased significantly. The initial G' values increased to approximately 3998.56 Pa for 0% starch, 6248.78 Pa for 2.5% starch, and 8891.23 Pa for 5% starch. This represents about a 90–100-fold increase compared with the untreated samples. The increase suggests that heating promoted the formation of a stronger internal network through interactions among the BSFP protein, TS, and GG. During heating, BSFP proteins may unfold and expose reactive groups, allowing for aggregation through hydrophobic interactions, hydrogen

bonding, and possible disulfide or other covalent linkages, depending on the amino acid composition.[30] At the same time, TS granules can swell and gelatinize, releasing amylose and increasing hydrogen bonding with water, proteins, and GG.[31] Gellan gum can also contribute to network formation through ordered chain association and junction-zone formation, supported by hydrogen bonding and possible ionic interactions with minerals present in the BSFP matrix.[32] Therefore, the thermally treated paste likely formed a combined protein–starch–hydrocolloid network, explaining the large increase in modulus and the improved structural stability expected during 3D printing.

The frequency sweep also showed that G' remained higher than G" across 0.1 – 100 rad/s, confirming a gel-like behavior in all samples. After heating, the higher-starch formulations showed stronger moduli, indicating greater network reinforcement. This is relevant to 3D printing because food inks with higher elastic modulus and suitable yield behavior generally show better shape retention and reduced post-deposition deformation. Overall, thermal treatment converted the BSFP paste from a weak structured paste into a stronger gel-like material, while starch level controlled the extent of reinforcement.

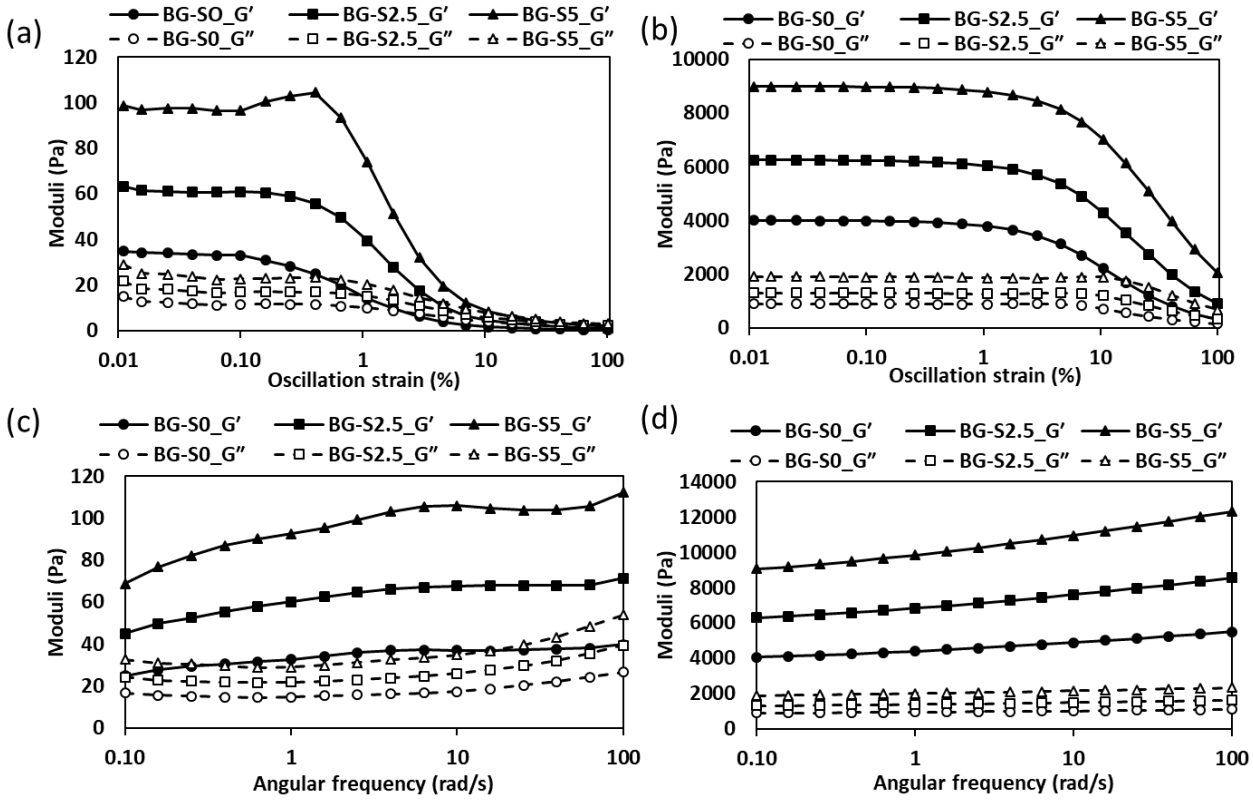

Figure 4. Strain and frequency sweep behavior of BSFP-based pastes containing 0, 2.5, and 5% tapioca starch: (a, c) before and (b, d) after thermal treatment.

3.2.2 Steady shear flow behavior of BSFP-based paste before and after thermal treatment

The untreated BSFP-based pastes showed clear shear-thinning behavior, as viscosity decreased with increasing shear rate (Figure 5a). The viscosity increased with starch level, from approximately 14 Pa·s for BG-S0 to about 40 Pa·s for BG-S5. This indicates that TS increased low-shear flow resistance and paste consistency. The shear stress of the untreated samples increased continuously with shear rate (Figure 5b), reaching 4.92, 8.83, and 14.65 Pa for BG-S0, BG-S2.5, and BG-S5 at 100 s^{-1}, respectively. This pattern suggests that the untreated samples behaved as weak structured dispersions, where the applied shear mainly increased deformation resistance.

The Herschel–Bulkley parameters supported this trend (Table 3). The model-estimated yield stress, τ_0, increased from 0.895 Pa for BG-S0 to 1.240 Pa for BG-S2.5 and 2.618 Pa for BG-S5. The consistency coefficient, K, also increased from 0.370 to 1.011, confirming that starch

increased resistance to flow. The flow behavior index, n, remained below 1 for all untreated samples, ranging from 0.518 to 0.540. This confirms shear-thinning behavior. The high R^2 values of 0.9861–0.9917 and low RMSE values of 0.155–0.416 show that the Herschel–Bulkley model described the untreated samples well.

After thermal treatment, viscosity increased greatly, especially at low shear rate (Figure 5c). At 0.1 s^{-1}, viscosity increased to 3349.28, 4399.74, and 6041.51 Pa·s for BG-S0, BG-S2.5, and BG-S5, respectively. This increase indicates heat-induced structure formation. BSFP proteins can form gel systems, and their functionality has been linked to changes in surface hydrophobicity and network development.[30] During heating, protein unfolding can expose hydrophobic groups and reactive sites. This can promote hydrophobic association, hydrogen bonding, and possible covalent cross-linking. Similar gelation behavior has been reported for mealworm protein, where hydrophobic interactions and hydrogen bonding were important contributors to heat-induced gel formation.[33]

The model-estimated τ_0 values of the thermally treated samples were much higher than those of the untreated samples. They increased to 363.577, 466.823, and 636.062 Pa for BG-S0, BG-S2.5, and BG-S5, respectively. This shows that thermal treatment produced a stronger network that required greater stress to initiate flow. The n values decreased to 0.233–0.259, indicating stronger shear-thinning behavior after heating. This is useful for 3D printing because the paste can maintain structure at rest but flow under nozzle shear. However, the fitted K values for the thermally treated samples were negative. This does not indicate an absolute negative consistency of the paste. Instead, it shows that the thermally treated stress data did not follow a simple monotonic Herschel–Bulkley pattern. The heated samples showed stress reduction and breakdown at higher shear rates, which violates the normal assumption of the model. Therefore, the negative K values should be treated as fitting artifacts and interpreted cautiously. The lower R^2 values of 0.9004–0.9204 and higher RMSE values also confirm that the model fit was weaker for the thermally treated samples than for the untreated samples.

The stress response of the thermally treated samples differed clearly from the untreated samples. Stress slightly decreased between 0.1 and 0.2 s^{-1}, remained relatively stable until about 0.6 s^{-1}, increased to a starch-dependent peak around 2.5 s^{-1}, and then declined at higher shear rates (Figure 5d). This suggests that the heated samples had a pre-formed gel network. Under shear, this network first resisted deformation, then rearranged, reached maximum resistance, and finally

broke down. The higher peak stress in BG-S5 indicates stronger reinforcement from starch gelatinization and GG network formation. GG can form a network through double-helix formation and aggregation, often promoted by cations.[34] Starch gelatinization can also increase viscosity through granule swelling and amylose leaching, which may strengthen interactions with proteins and hydrocolloids.

This explains why the stress peak was observed only after thermal treatment. Before heating, the paste behaved mainly as a weak dispersion, so stress increased with shear rate. After heating, the protein–starch–GG matrix formed a stronger gel-like network that could resist deformation before structural breakdown. For 3D printing, this behavior is important because the paste should resist deformation after deposition but flow when sufficient shear is applied through the nozzle. Similar rheology–printability relationships were reported for complex food inks containing insect flour and orange peel by-products, where starch concentration and printing temperature affected flow behavior, extrusion quality, and printed-shape stability.[35] In another food-ink study, yield stress was strongly related to printing force, while shear-thinning behavior supported extrusion under pressure.[36]

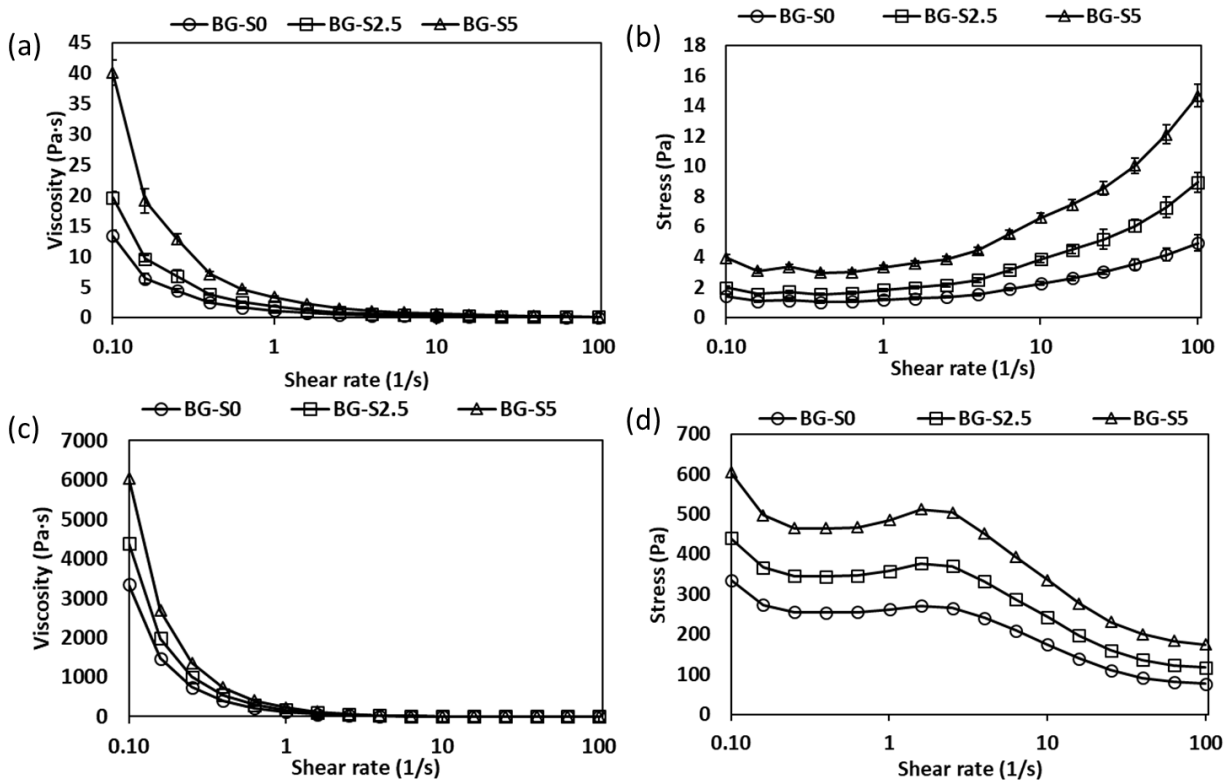

Figure 5. Steady shear behavior of BSFP-based pastes containing different tapioca starch levels before and after thermal treatment. (a) Apparent viscosity and (b) shear stress of untreated samples; (c) apparent viscosity and (d) shear stress of thermally treated samples.

Table 3. Herschel–Bulkley model parameters for BSFP-based pastes before and after thermal treatment.

	Sample code					
	Before thermal treatment			After thermal treatment		
	BG-S0	**BG-S2.5**	**BG-S5**	**BG-S0**	**BG-S2.5**	**BG-S5**
τ_0	0.895	1.240	2.618	363.577	466.823	636.062
K	0.370	0.714	1.011	-107.070	-117.332	-161.220
n	0.523	0.518	0.540	0.233	0.259	0.248
SSE	0.313	0.655	2.254	8017.03	15066.0	28146.0
R^2	0.9861	0.9917	0.9885	0.9204	0.9099	0.9004
RMSE	0.155	0.224	0.416	24.833	34.043	46.530

BG-S0, BG-S2.5, and BG-S5 represent BSFP-based pastes containing 0, 2.5, and 5% tapioca starch, respectively. τ_0 is the model-estimated yield stress, K is the consistency coefficient, n is the flow behavior index, SSE is the sum of squared errors, and RMSE is the root mean square error.

3.2.3 Heat-induced structural development of BSFP-based paste during temperature sweep

The temperature sweep result showed that all BSFP-based pastes had low moduli during the early heating stage, followed by a rapid increase in G' and G" above approximately 65–70 °C (Figure 6). This temperature range indicates the onset of heat-induced structure development in the paste. The increase was formulation-dependent, with BG-S5 showing the highest modulus, followed by BG-S2.5 and BG-S0. At the final heating stage, G' reached approximately 3600 Pa for BG-S0, 5200 Pa for BG-S2.5, and 7800 Pa for BG-S5, confirming that TS increased the strength of the thermally formed network.

This behavior supports the results obtained after water-bath treatment, where the heated samples showed higher modulus, viscosity, and yield-related resistance. The sharp increase in G' during heating suggests that the structural transition occurred mainly during the heating process rather than only after cooling. This transition was likely associated with combined protein

denaturation, starch swelling or gelatinization, and GG-assisted network formation, as reported for insect protein gels, starch-based food printing systems, and GG gels.[13,30,33,34]

Overall, the temperature sweep confirmed that thermal treatment changed the BSFP-based paste from a weakly structured system into a stronger gel-like matrix. This heat-induced strengthening is important for 3D printing because it can improve post-extrusion shape retention. However, the stronger response of BG-S5 also suggests that excessive reinforcement may increase extrusion resistance and die swell.

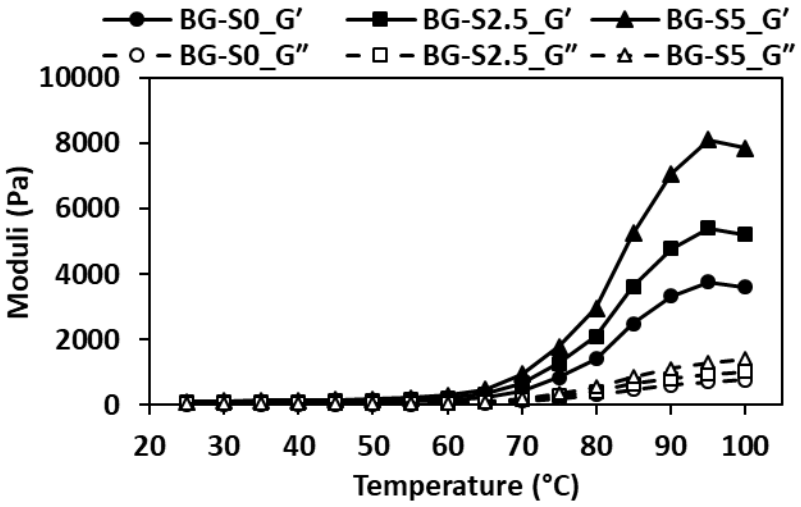

Figure 6. Temperature sweep behavior of BSFP-based pastes containing different tapioca starch levels.

3.2.4 Nonlinear viscoelastic behavior of BSFP-based paste under large deformation

The nonlinear viscoelastic behavior of the BSFP-based pastes is shown in Figure 7. At low strain amplitudes of 0.5–10%, the Lissajous curves were narrow and nearly elliptical, showing that the samples were close to the linear viscoelastic region (Figure 7a,b). From about 50% strain, the curves became wider, and clear nonlinear deformation was observed between 100 and 1000% strain. This indicates progressive structural deformation under large oscillatory strain. LAOS is useful for this interpretation because Lissajous curves can reveal nonlinear responses such as structural breakdown, strain stiffening, and shear thinning, which are not fully described by small-amplitude measurements.[27,37]

The stress response increased with TS concentration. BG-S5 showed the largest loops, followed by BG-S2.5 and BG-S0 (Figure 7a,b). At 1000% strain, the stress range increased from approximately ±25 Pa in BG-S0 to about ±250 Pa in BG-S2.5 and nearly ±780 Pa in BG-S5. This confirms that TS increased resistance to large deformation. The wider stress–strain loops of BG-S5 also suggest greater energy dissipation and stronger nonlinear elastic resistance (Figure 7b). This agrees with the SAOS and steady shear results, where higher TS content increased modulus, viscosity, and yield-related resistance.

The individual component analysis supports this interpretation (Figure S2). BSFP-only showed the weakest LAOS response, with stress mostly within approximately ±6 Pa, indicating limited resistance to large deformation (Figure S2a,b). TS-only showed a stronger response and reached about ±2000 Pa at high strain, while GG-only showed the highest stress response, approaching ±10,000 Pa. This shows that GG was the main network-forming component, while TS acted as a structural reinforcement. Although BSFP proteins have techno-functional and gel-forming potential, their behavior depends strongly on processing and formulation conditions.[24,30]

The effect of moisture content on BSFP-only paste was also considered to support the selected base condition (Figure S3). The 75% moisture sample showed the highest BSFP-only stress response, reaching about ±45 Pa at high strain. However, this lower-moisture condition may reduce the available water needed for complete hydration and uniform dispersion of GG and TS. As moisture increased to 90%, the stress response decreased strongly, and the 90% sample showed very weak loops, mostly below ±0.5 Pa. The 80% moisture sample gave an intermediate response. Therefore, 80% moisture was selected because it provided a practical balance between BSFP solid content, hydration capacity, and structural response under large deformation.

Overall, the LAOS results show that BSFP alone was not sufficient to provide strong nonlinear resistance after deformation. This supports the need to combine BSFP with GG and TS for extrusion-based 3D printing. BSFP provides the protein-rich base, GG contributes strong network formation, and TS improves deformation resistance and structural stability. Similar LAOS studies on structured food systems have shown that nonlinear deformation behavior is strongly affected by composition and matrix structure.[38] Increasing TS changed the paste from a weak nonlinear material into a more deformation-resistant matrix. However, the strong response of BG-

S5 suggests that excessive reinforcement may increase elastic recovery and die swell. Therefore, BG-S2.5 may provide a more balanced response between flow, deformation, and structural recovery.

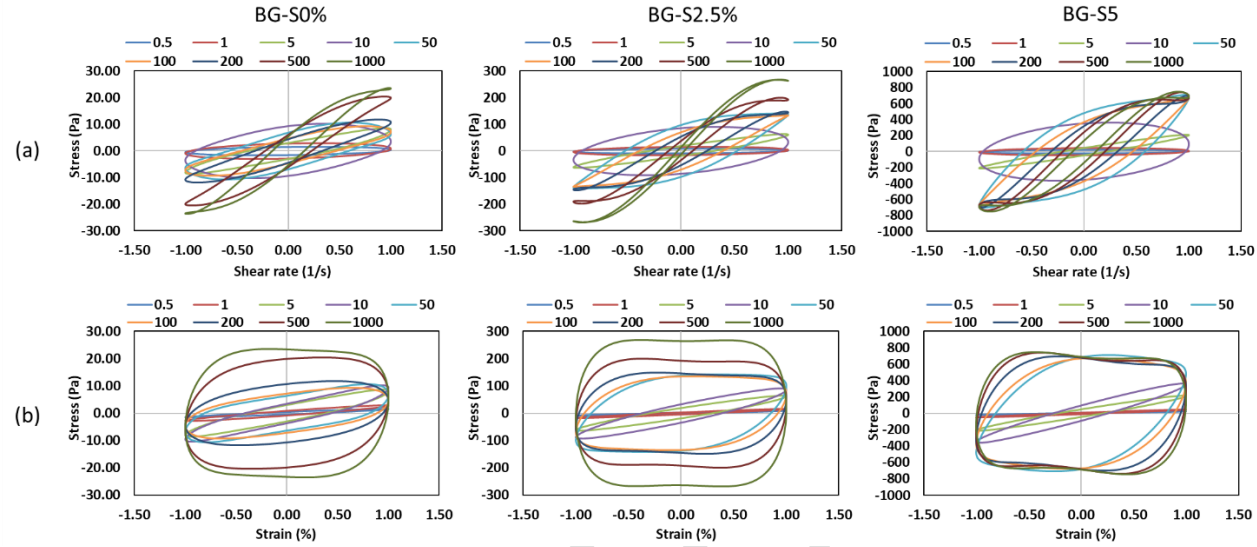

Figure 7. LAOS response of BSFP-based pastes containing different tapioca starch levels. (a) Stress–shear rate Lissajous curves and (b) stress–strain Lissajous curves of BG-S0, BG-S2.5, and BG-S5 measured at strain amplitudes of 0.5–1000%.

3.2.5 Chebyshev analysis of nonlinear elastic and viscous responses

The Chebyshev coefficients provided a clearer interpretation of the nonlinear behavior observed in the LAOS curves. At low strain amplitudes, the e_3/e_1, v_3/v_1, S, and T values of the BSFP-based pastes were close to zero, confirming that the samples were near the linear viscoelastic region (Figure 8). As strain increased above approximately 50–100%, the nonlinear coefficients changed markedly, showing that the internal structure was being deformed under large oscillatory strain. These parameters are useful because positive e_3/e_1 and S indicate intra-cycle strain stiffening, while negative v_3/v_1 and T indicate intra-cycle shear thinning.[27,29]

The elastic nonlinear response increased with TS concentration. In BG-S0, e_3/e_1 remained low until high strain and increased to about 0.45 at 1000% strain (Figure 8a). In contrast, BG-S2.5 and BG-S5 increased more strongly, reaching about 0.80 and 1.05, respectively. The same trend

was observed for S, where BG-S5 showed the highest strain stiffening, followed by BG-S2.5 and BG-S0 (Figure 8c). This indicates that TS reinforced the BSFP-based matrix and increased resistance during large deformation. Similar LAOS behavior has been reported in dough systems, where strain stiffening was linked to the elastic network and shear thinning to rearrangement of the dispersed starch phase.[39]

The viscous nonlinear response showed a different pattern. BG-S0 had negative v_3/v_1 and T values that became more negative as strain increased, reaching about −0.25 and −0.90, respectively (Figure 8b,d). This indicates strong intra-cycle shear thinning and structural breakdown. BG-S2.5 and BG-S5 showed small positive viscous values at intermediate strain, followed by negative values at higher strain. This suggests that the starch-containing samples first resisted deformation through temporary structure formation, but later showed shear thinning as the network was disrupted. Ewoldt *et al.*[27] described negative v_3 and T values as indicators of intra-cycle shear thinning, while positive values indicate shear thickening.

The individual component results explain the origin of these trends (Figure S4). GG-only showed the strongest elastic nonlinearity, with e_3/e_1 and S increasing strongly at high strain, confirming its role as the main network-forming component. TS-only remained close to zero for most coefficients, indicating limited nonlinear structure when tested alone. BSFP-only showed unstable viscous behavior, where v_3/v_1 and T first decreased strongly into the negative region and then increased again at higher strain. This suggests that the weak BSFP structure initially broke down under deformation, after which the response became more controlled by flow alignment and particle rearrangement. BSFP proteins have been reported to show functional and gel-forming potential, but their behavior depends strongly on processing and formulation conditions.[30]

The BSFP-only moisture series further supports the selection of 80% moisture for the combined formulation (Figure S5). The 75% sample showed the strongest elastic response at high strain, while 90% moisture sample showed the weakest structural response and the largest negative S and T values at intermediate strain. The 80% sample showed a more balanced response, with moderate elastic nonlinearity and less severe structural weakening than the 85 and 90% samples. This suggests that 80% moisture provided enough water for hydration and dispersion of GG and TS while maintaining sufficient BSFP structural contribution.

Overall, the Chebyshev analysis confirms that BSFP alone cannot provide stable nonlinear resistance under large deformation. GG supplied the main elastic network, while TS increased strain stiffening and deformation resistance. This combination is important for extrusion-based 3D printing because the paste must shear-thin during nozzle flow but recover enough structure after deposition. The stronger response of BG-S5 may improve shape retention but can also promote elastic recovery and die swell, whereas BG-S2.5 provided a more balanced nonlinear response for controlled printing.

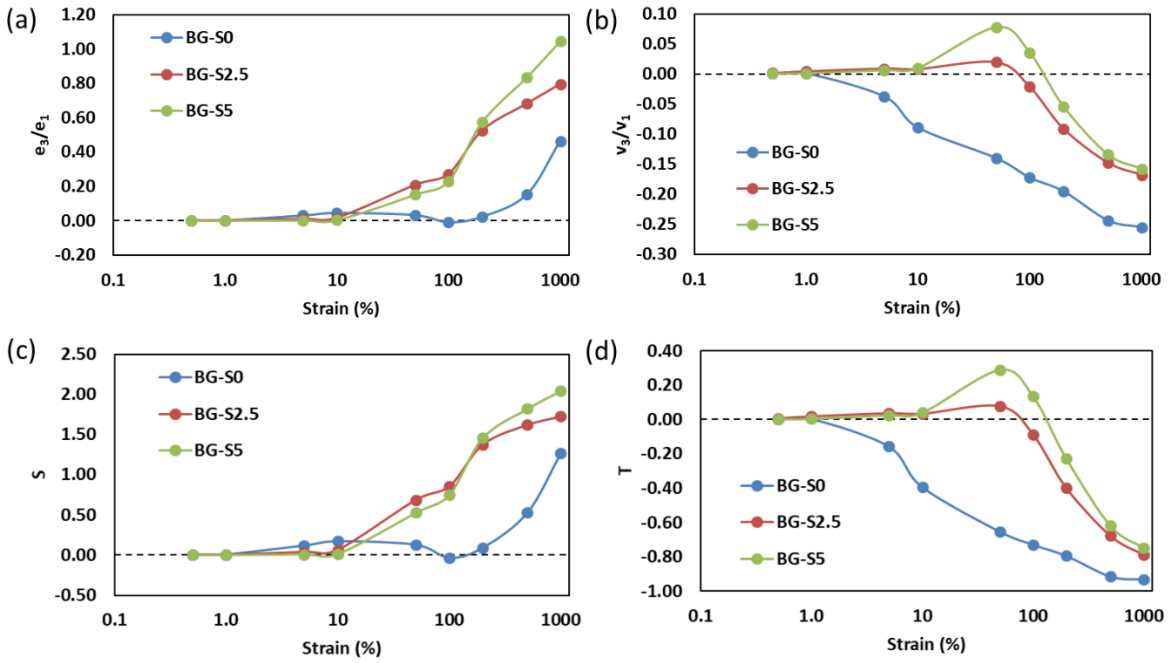

Figure 8. Chebyshev coefficient analysis of BSFP-based pastes containing different tapioca starch levels under large-amplitude oscillatory shear. (a) Elastic nonlinearity ratio, e_3/e_1; (b) viscous nonlinearity ratio, v_3/v_1; (c) strain stiffening ratio, S; and (d) shear thickening ratio, T.

3.3 Image-based analysis of die swell and filament uniformity of 3D-printed BSFP extrudates

The die swell and filament uniformity of the BSFP-based extrudates are shown in Figure 9. The mean die swell ratio increased with TS concentration, from approximately 1.63 for BG-S0 to 1.69 for BG-S2.5 and 1.96 for BG-S5 (Figure 9c). This shows that the printed filament diameter

became larger than the 1.2 mm nozzle diameter after extrusion. Die swell is commonly associated with elastic recovery after a viscoelastic material exits the nozzle, and the swell ratio is often used as a geometric indicator of elastic recoil at the nozzle tip.[6,40]

The higher die swell ratio in BG-S5 agrees with the rheological results. BG-S5 had the highest modulus, yield-related resistance, and LAOS stress response, indicating a stronger and more elastic internal network. During nozzle flow, this network is deformed and aligned. After exiting the nozzle, part of the stored elastic energy is released, causing radial expansion of the filament. This explains why higher TS concentration produced greater die swell. Similar relationships between food ink composition, rheology, and extrusion behavior have been reported, where rheological properties strongly affected filament spreading, extrusion quality, and printed shape stability.[9,41]

The edge roughness result showed that BG-S2.5 had the lowest mean edge roughness, approximately 0.049 mm, while BG-S0 and BG-S5 showed higher values of about 0.060 mm and 0.074 mm, respectively (Figure 9a). This indicates that BG-S2.5 produced the smoothest filament edge. BG-S0 had lower die swell but weaker structural support, which may have caused less uniform filament boundaries. In contrast, BG-S5 had a stronger structure but higher elastic recovery, leading to greater edge irregularity after extrusion.

The thickness variation result followed the same trend. BG-S2.5 had the lowest thickness CV, approximately 8.1%, while BG-S0 and BG-S5 were both above 10% (Figure 9b). This suggests that BG-S2.5 produced the most uniform filament thickness along the printed length. In extrusion-based food printing, a stable filament requires a balance between flowability and shape retention. Materials that are too weak may spread after deposition, while highly elastic materials may show stronger die swell and dimensional variation.[42]

Overall, BG-S2.5 showed the best balance between die swell, edge smoothness, and filament uniformity. BG-S5 had the highest die swell and roughness due to stronger elastic recovery, while BG-S0 had weaker structural stability. These results support the rheological interpretation that moderate TS addition improved printing quality, whereas excessive reinforcement increased die swell and reduced dimensional uniformity.

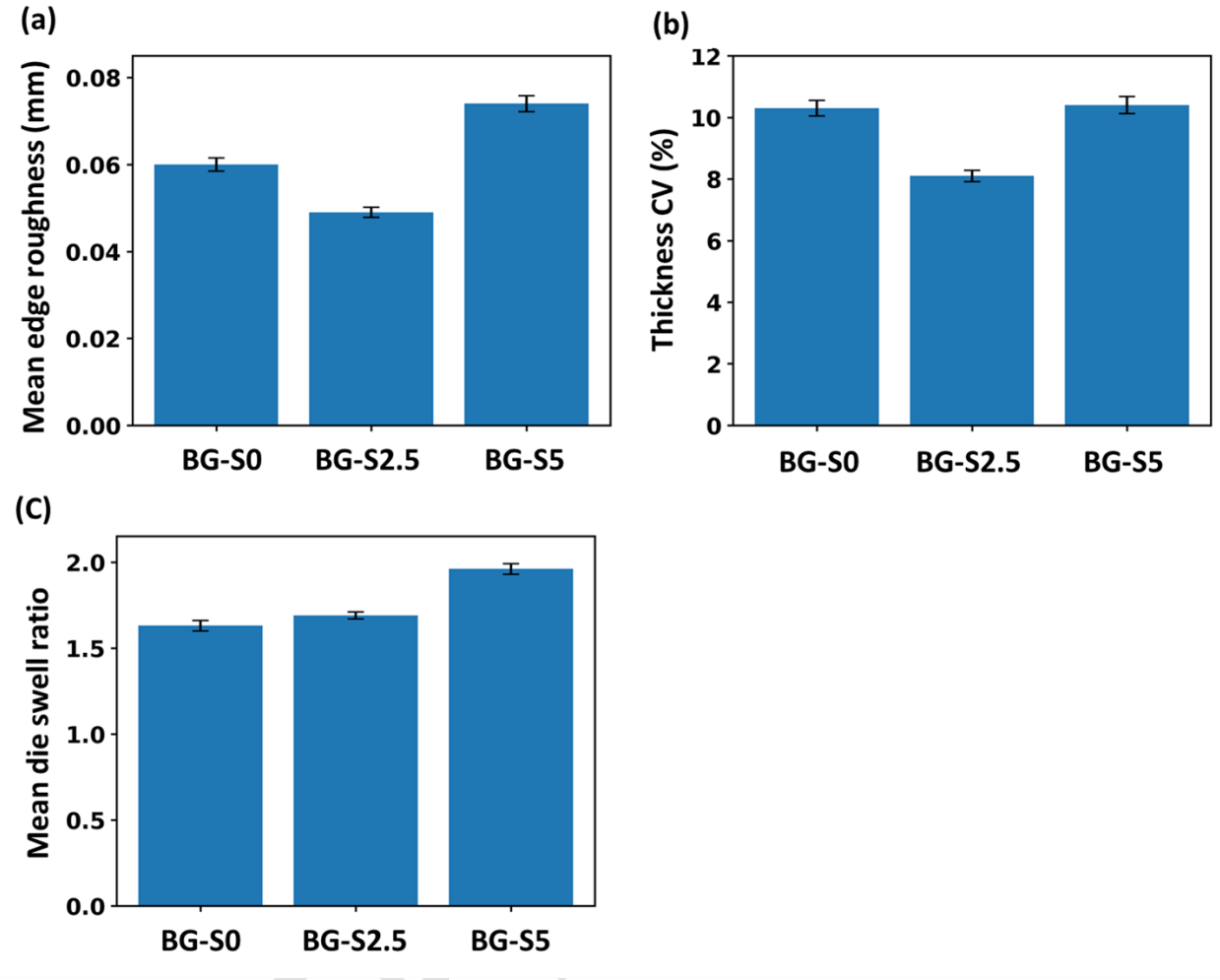

Figure 9. Image-based evaluation of filament quality and die swell of 3D-printed BSFP-based extrudates. (a) Mean edge roughness, (b) thickness coefficient of variation, and (c) mean die swell ratio of BG-S0, BG-S2.5, and BG-S5 extrudates printed using a 1.2 mm nozzle.

3.4 Printing performance and post-printing stability of BSFP-based formulations

The printing behavior of the BSFP-based formulations is shown in Figure 10, while the quantitative shape-fidelity and stability results are presented in Table 4. BG-S0 showed poor layer stacking and substantial spreading during printing. After 10 min, the printed structure lost its square geometry and collapsed, which was reflected in the lowest overall shape fidelity of 58.81% and height retention of 53.80%. It also showed the highest post-print spreading and structural deformation, at 15.71% and 30.96%, respectively.

BG-S2.5 produced continuous filaments, supported stable layer deposition, and maintained a well-defined open-box structure after printing. Its overall shape fidelity reached 92.34%, with height retention of 97.26% and 0.67% post-print spreading. These results agree with its lower filament roughness and thickness variation, confirming that the moderate tapioca starch concentration provided a suitable balance between extrusion flow and structural recovery.

BG-S5 also retained its printed height and showed low post-print deformation. However, its wall-thickness accuracy and overall shape fidelity were lower than those of BG-S2.5, indicating that the stronger paste structure and greater die swell produced thicker and less uniform deposited layers. The TS-only sample showed the highest dimensional accuracy and post-print stability, confirming the strong structural contribution of gelatinized starch. Among the BSFP-containing formulations, BG-S2.5 therefore provided the best overall printing performance by combining high dimensional fidelity, low spreading, and stable shape retention.

Because full-fat BSFP powder is a heterogeneous particulate material with limited water solubility and a broad particle-size distribution, printing thin unsupported features is more challenging than in homogeneous starch- or protein-isolate-based inks. The open-box model was therefore initially selected to assess continuous extrusion, multilayer deposition, vertical wall formation, and post-print stability without introducing extensive unsupported spans. To further validate the practical printability of the selected formulation, BG-S2.5 was subsequently used to print a more complex 20 × 20 × 20 mm perforated box containing repeated square openings, as shown in Figure S6. The first two rows of perforations were formed without obvious deformation. However, when the printed height exceeded 12.89 ± 0.45 mm, the openings in the lowest row gradually narrowed because of the increasing load imposed by the newly deposited layers. Despite this progressive deformation, the structure retained its overall three-dimensional form at the end of printing. This result confirms that BG-S2.5 can produce a more demanding complex geometry, while also showing that further optimization is required to improve pore fidelity in taller structures.

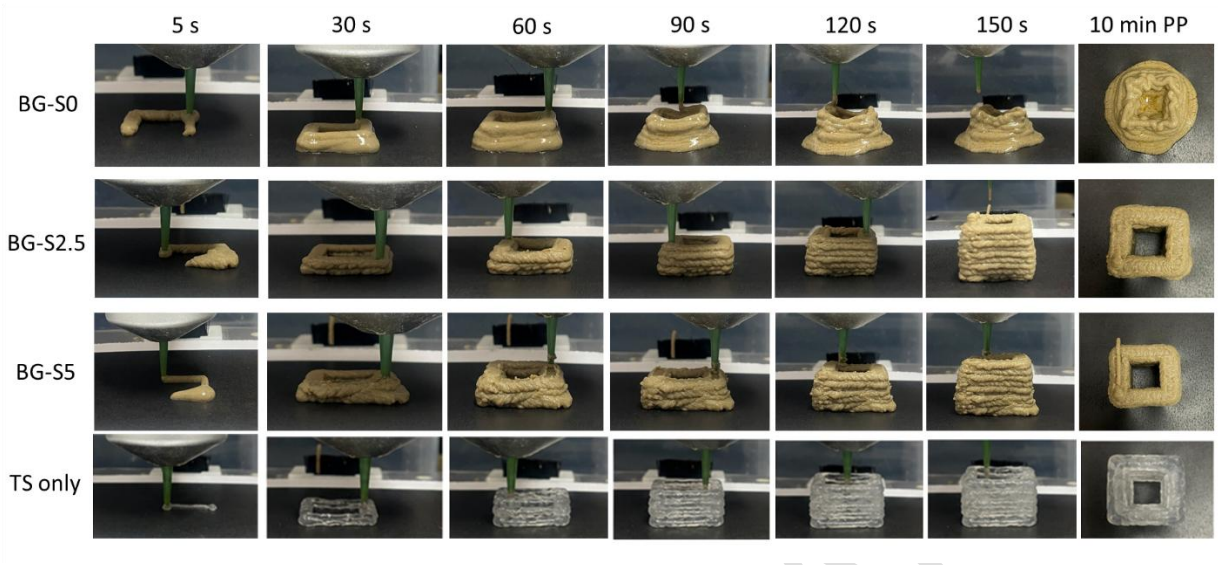

Figure 10. Time-sequence images of 3D printing and post-printing stability of BSFP-based formulations and TS-only sample. Images were captured during printing at 5, 30, 60, 90, 120, and 150 s, and after 10 min post-printing (10 min PP) to evaluate filament deposition, layer stacking, shape formation, and structural stability.

Table 4. Shape fidelity and post-print structural stability of 3D-printed BSFP-based structures

Sample	Height fidelity (%)	Width accuracy (%)	Wall-thickness accuracy (%)	Overall shape fidelity (%)	Height retention (%)	Post-print spreading (%)	Structural deformation (%)
BG-S0	70.00 ± 1.41^{c}	74.77 ± 2.83^{c}	31.67 ± 4.02^{c}	58.81 ± 2.60^{c}	53.80 ± 1.13^{b}	15.71 ± 1.34^{a}	30.96 ± 0.54^{a}
BG-S2.5	95.95 ± 0.96^{a}	95.92 ± 0.48^{ab}	85.14 ± 3.78^{a}	92.34 ± 1.08^{a}	97.26 ± 0.72^{a}	0.67 ± 0.10^{b}	1.71 ± 0.40^{b}
BG-S5	92.23 ± 1.08^{b}	92.88 ± 1.80^{b}	66.94 ± 1.97^{b}	84.02 ± 1.41^{b}	97.85 ± 0.12^{a}	0.56 ± 0.30^{b}	1.36 ± 0.20^{bc}
TS only	97.57 ± 0.48^{a}	97.70 ± 0.56^{a}	89.44 ± 3.54^{a}	94.90 ± 1.27^{a}	98.57 ± 0.05^{a}	0.08 ± 0.03^{b}	0.76 ± 0.04^{c}

Values are expressed as mean ± standard deviation of three independently printed structures. Different superscript lowercase letters within the same column indicate significant differences ($p<0.05$) among formulations.

3.5 Microstructural characteristics of BSFP-based formulations

The SEM micrographs revealed clear differences between the BSFP powder and the thermally treated BSFP-based formulations (Figure 11). The BSFP-only sample consisted of irregular, loosely connected agglomerates with numerous interparticle voids and elongated fibre-like fragments. The absence of a continuous surrounding phase confirmed the heterogeneous particulate nature of the full-fat powder and helps explain its limited ability to form a cohesive and deformation-resistant paste without additional structuring ingredients.

In contrast, BG-S0 exhibited a comparatively smooth and continuous surface containing fused rounded domains and fewer open spaces. This observation indicates that gellan gum and thermal treatment promoted particle coating and matrix continuity. Nevertheless, the relatively homogeneous surface showed limited evidence of extensive structural reinforcement. Although BG-S0 formed a continuous dried matrix, its low rheological strength and poor printing fidelity indicate that surface continuity alone was insufficient to prevent spreading and structural collapse during and after printing. On the other hand, BG-S2.5 formulation displayed a continuous but moderately heterogeneous matrix in which BSFP-derived domains appeared embedded and connected by the surrounding starch–gellan phase. Small pits, shallow cavities, and particle–matrix bridges were visible, but the structure was less densely aggregated than BG-S5. This intermediate morphology suggests improved integration among the BSFP particles, gelatinized tapioca starch, and gellan gum without excessive network compaction. The resulting balance between matrix continuity and controlled structural heterogeneity agrees with the lower filament edge roughness, reduced thickness variation, high shape fidelity, and good post-print stability of BG-S2.5.

BG-S5 showed the roughest and most strongly aggregated morphology, with compact fused regions, irregular cavities, folded surfaces, and densely interconnected particle clusters. The increased degree of aggregation is consistent with greater starch gelatinization and more extensive association of the starch-rich continuous phase with BSFP particles and gellan gum. This strongly reinforced morphology supports the higher storage modulus, yield-related resistance, strain stiffening, hardness, and height retention of BG-S5. However, the dense and heterogeneous

structure may also store greater elastic energy during nozzle flow, thereby contributing to the higher die-swell ratio, rougher filament edges, and reduced wall-thickness accuracy.

Overall, the SEM observations were consistent with the rheological and printing results, showing formulation-dependent differences in matrix continuity, particle integration, and aggregation. BG-S2.5 exhibited a moderately integrated structure, while BG-S5 showed more pronounced aggregation and structural heterogeneity.

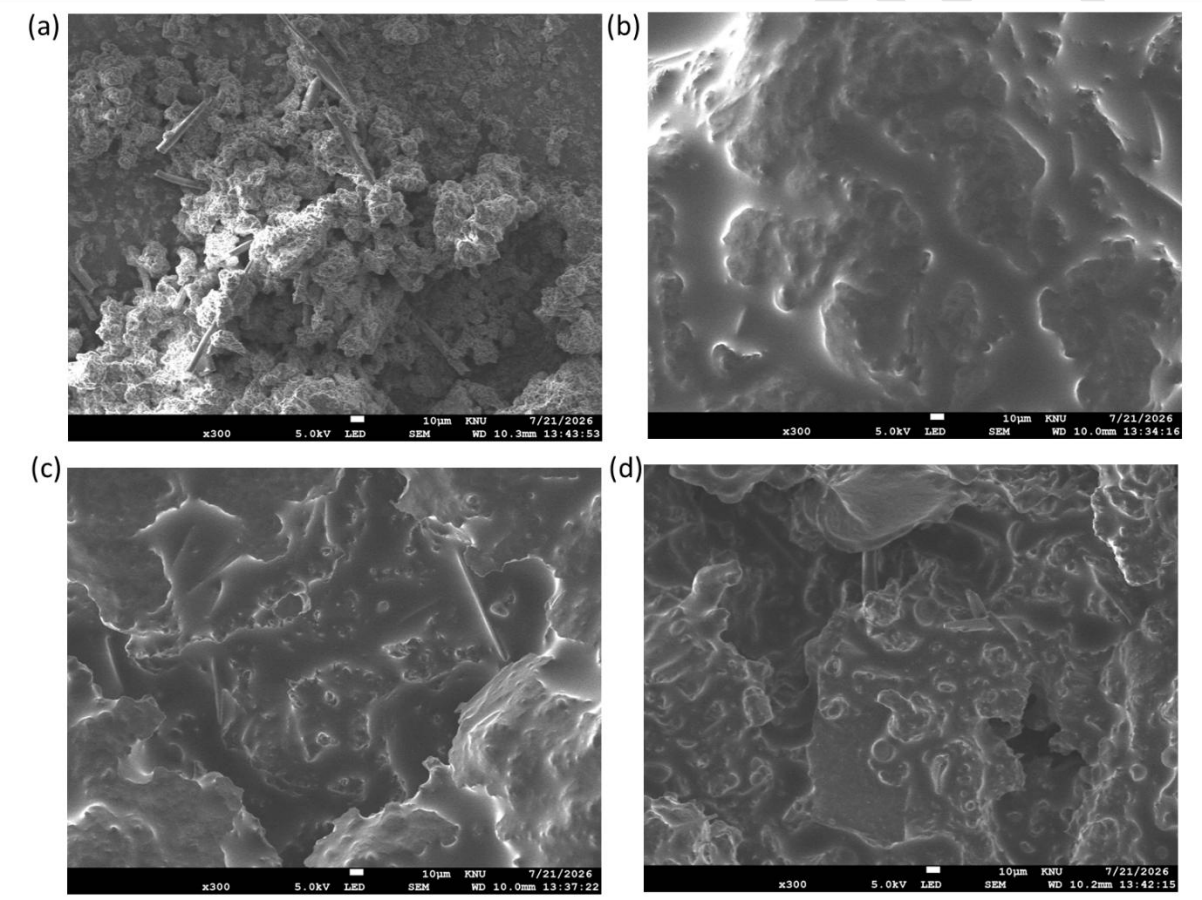

Figure 11. Scanning electron micrographs of the full-fat BSFP powder and thermally treated BSFP-based formulations at ×300 magnification: (a) BSFP only, (b) BG-S0, (c) BG-S2.5, and (d) BG-S5.

3.6 Texture properties of the printed structures

The texture profile analysis results of the printed BG-S2.5, BG-S5, and TS-only structures are presented in Table 5. BG-S5 showed the highest hardness, adhesiveness, gumminess, and chewiness, indicating that the higher starch concentration produced a stronger and more deformation-resistant printed structure. This result agrees with its higher viscoelastic modulus and greater resistance to large deformation, although its increased mechanical strength was also associated with greater die swell and lower wall-thickness accuracy.

BG-S2.5 had the lowest hardness, gumminess, and chewiness, indicating a softer printed structure. Nevertheless, it maintained high-dimensional fidelity and post-print stability, showing that moderate mechanical strength was sufficient to support the deposited layers without producing excessive stiffness or elastic recovery. The TS-only sample showed the highest springiness, cohesiveness, and resilience, suggesting greater elastic recovery and internal structural integrity. Overall, BG-S2.5 provided a comparatively softer texture while maintaining good printing accuracy, whereas BG-S5 produced the strongest but more rigid BSFP-based structure.

Table 5. Texture properties of 3D printed BSFP-based structures and the tapioca starch control

Sample	BG-S2.5	BG-S5	TS only
Hardness (N)	8.18 ± 0.16^{c}	13.52 ± 0.26^{a}	10.21 ± 0.21^{b}
Adhesiveness (N·s)	1.77 ± 0.07^{b}	2.35 ± 0.10^{a}	1.47 ± 0.07^{c}
Springiness	0.82 ± 0.02^{c}	0.88 ± 0.02^{b}	0.91 ± 0.02^{a}
Cohesiveness	0.62 ± 0.01^{c}	0.68 ± 0.01^{b}	0.72 ± 0.01^{a}
Gumminess (N)	5.04 ± 0.19^{c}	9.14 ± 0.32^{a}	7.31 ± 0.27^{b}
Chewiness (N)	4.13 ± 0.23^{c}	8.05 ± 0.42^{a}	6.66 ± 0.35^{b}
Resilience	0.25 ± 0.01^{c}	0.32 ± 0.01^{b}	0.36 ± 0.01^{a}

Values are expressed as mean ± standard deviation of five independently printed structures. Different superscript lowercase letters within the same row indicate significant differences ($p<0.05$) among formulations.

4. Conclusion

This study developed a full-fat black soldier fly prepupal (BSFP) powder-based paste for direct ink writing and clarified how thermal treatment and tapioca starch concentration affected its rheology, extrusion behavior, texture, and printing performance. The BSFP powder showed limited water solubility and a broad particle-size distribution, confirming its heterogeneous particulate nature and the need for additional matrix-forming ingredients. Preliminary rheological screening identified 7.5% BSFP and 0.5% gellan gum (GG) as suitable initial base conditions. Based on these results, the final formulations were prepared at approximately 80% moisture with 0, 2.5, or 5% tapioca starch (TS), while GG was maintained at 0.5% and the BSFP powder and water contents were adjusted accordingly. Thermal treatment markedly increased the viscoelastic strength, viscosity, and yield behavior of all formulations through heat-induced network development. LAOS and Chebyshev analyses further showed that increasing starch concentration enhanced nonlinear elastic resistance and strain stiffening. SEM observations further showed formulation-dependent differences in matrix continuity, particle integration, and aggregation, supporting the rheological and printing results. However, the strongest formulation was not the most printable. BG-S5 showed the greatest elastic recovery, die swell, hardness, gumminess, and chewiness, but also produced thicker, rougher, and less dimensionally accurate filaments. BG-S2.5 provided the best balance between flowability and structural recovery. It produced the lowest filament edge roughness and thickness variation, an overall shape fidelity of 92.34%, height retention of 97.26%, and 0.67% post-print spreading. It also maintained a comparatively softer texture than BG-S5 while supporting stable multilayer deposition. Additional printing of a perforated box confirmed its ability to form a more complex structure with repeated openings, although progressive narrowing of the lower perforations occurred when the structure height exceeded 12.89 ± 0.45 mm. Overall, 2.5% tapioca starch was the optimal level for balancing rheological strength, die-swell control, dimensional fidelity, texture, and post-print stability in BSFP-based pastes.

Acknowledgments
This study was partially supported by Jae Park Surimi School. All authors would like to express their gratitude to Randy H. Ewoldt from University of Illinois at Urbana-Champaign for providing free access to the MITLaos software (MITlaos Version 2.1 Beta).

Funding
This research has received funding support from the National Science, Research and Innovation Fund (NSRF) via the Program Management Unit for Human Resources & Institutional Development, Research and Innovation (grant number B38G670001), Thailand. Additional funding was also supported by the Basic Science Research Program through the National Research Foundation of Korea (NRF), funded by the Ministry of Education (NRF2018R1D1A3B06042501). The support from the ANCHOR program through the Gangwon ANCHOR Center, funded by the Ministry of Education (MOE) and the Gangwon State (G.S.), Republic of Korea (2026-ANCHOR-10-002), was greatly appreciated.

Conflict of interest
The authors declare they have no competing interests.

Author contributions
Conceptualization: Timilehin Martins Oyinloye, Jirawat Yongsawatdigul, Won Byong Yoon
Formal analysis: Timilehin Martins Oyinloye, Yupa Hanboonsong
Funding acquisition: Jirawat Yongsawatdigul, Won Byong Yoon
Investigation: Timilehin Martins Oyinloye, Sununta Chumee
Methodology: Timilehin Martins Oyinloye, Yupa Hanboonsong, Won Byong Yoon
Supervision: Won Byong Yoon
Writing–original draft: Timilehin Martins Oyinloye
Writing–review & editing: Jirawat Yongsawatdigul, Won Byong Yoon

Ethics approval and consent to participate
Not applicable.

Consent for publication
Not applicable.

Availability of data
The data presented in this study are available on request from the corresponding author. The data are not publicly available due to restrictions imposed by the funding agreement.

References

1. Lu S, Taethaisong N, Meethip W, *et al*. Nutritional composition of black soldier fly larvae (Hermetia illucens L.) and its potential uses as alternative protein sources in animal diets: A review. *Insects*. 2022;13(9):831. doi:10.3390/insects13090831.
2. Katemala K, Hanboonsong Y, Chumee S, *et al*. Rice bran and surimi by-products enhance nutritional quality and growth gene expression in Hermetia illucens (L.). *J Insects Food Feed*. Published online June 2026:1-21. doi:10.1163/23524588-bja10424.
3. Barragan-Fonseca KB, Gort G, Dicke M, van Loon JJA. Effects of dietary protein and carbohydrate on life-history traits and body protein and fat contents of the black soldier fly *Hermetia illucens*. *Physiol Entomol*. 2019;44(2):148-159. doi:10.1111/phen.12285.
4. Mshayisa VV. Physico-chemical, Techno-functional and Structural Properties of Native and Glycated Proteins Isolated From Black Soldier Fly (Hermetia illucens) Larvae. Doctoral dissertation. Bellville, South Africa: Cape Peninsula University of Technology; 2021. Accessed July 15, 2026. https://etd.cput.ac.za/server/api/core/bitstreams/c7b5c15b-9d84-41c5-b73f-ff6e9f592262/content
5. Hron B, Rosen R. Viscosity of commercial food-based formulas and home-prepared blenderized feeds. *J Pediatr Gastroenterol Nutr*. 2020;70(6):e124-e128. doi:10.1097/MPG.0000000000002657.
6. Oyinloye TM, Yoon WB. Impact of saturated and unsaturated oils on the nonlinear viscoelasticity, microstructure, and 3D printability of fish myofibrillar-protein-based pastes and gels. *Gels*. 2025;11(4):295. doi:10.3390/gels11040295.
7. Jeon EY, Kim Y, Yun HJ, Kim BK, Choi YS. 3D printing of materials and printing parameters with animal resources: A review. *Food Sci Anim Resour*. 2024;44(2):225-238. doi:10.5851/kosfa.2023.e73.
8. Tejada-Ortigoza V, Cuan-Urquizo E. Towards the development of 3D-printed food: A rheological and mechanical approach. *Foods.* 2022;11(9):1191. doi:10.3390/foods11091191.
9. Bugday ZY, Venkatachalam A, Anderson PD, van der Sman RGM. Rheology of paste-like food inks for 3D printing: Effects of nutrient and water content. *Curr Res Food Sci.* 2024;9:100847. doi:10.1016/j.crfs.2024.100847.
10. Kim HW, Lee JH, Park SM, *et al*. Effect of hydrocolloids on rheological properties and printability of vegetable inks for 3D food printing. *J Food Sci.* 2018;83(12):2923-2932. doi:10.1111/1750-3841.14391.
11. Hu H, Guo J, Huang Z, Huang Q, Lu X. Effect of different hydrocolloids on the physicochemical, printing, and digestion properties of 3D printed purple sweet potato. *Food Hydrocoll*. 2023;144:109058. doi:10.1016/j.foodhyd.2023.109058.
12. Oh Y, Lee S, Lee NK, Rhee JK. Improving the three-dimensional printability of potato starch loaded onto food ink. *J Microbiol Biotechnol*. 2024;34(4):891-901. doi:10.4014/jmb.2311.11040.
13. Toniazzo T, Leverrier C, Souza NL, Almeida G, Tadini CC, Guenard-Lampron V. Influence of starch-based gels on 3D food printing: Linking printability, texture,

rheological properties, and sensory evaluation. *Future Foods*. 2025;12:100725. doi:10.1016/j.fufo.2025.100725.
14. Yan B, Zhao Z, Zhang N, *et al*. 3D food printing curing technology based on gellan gum. *J Food Eng*. 2022;327:111036. doi:10.1016/j.jfoodeng.2022.111036.
15. Abdl Aali RAK, Al-Sahlany STG. Gellan gum as a unique microbial polysaccharide: Its characteristics, synthesis, and current application trends. *Gels*. 2024;10(3):183. doi:10.3390/gels10030183.
16. Campbell M, Ortuño J, Stratakos AC, *et al*. Impact of thermal and high-pressure treatments on the microbiological quality and in vitro digestibility of black soldier fly (*Hermetia illucens*) larvae. *Animals (Basel)*. 2020;10(4):682. doi:10.3390/ani10040682.
17. Bessa LW, Pieterse E, Marais J, Dhanani K, Hoffman LC. Food safety of consuming black soldier fly (*Hermetia illucens*) larvae: Microbial, heavy metal and cross-reactive allergen risks. *Foods*. 2021;10(8):1934. doi:10.3390/foods10081934.
18. Xu L, Gu L, Su Y, *et al*. Impact of thermal treatment on the rheological, microstructural, protein structures and extrusion 3D printing characteristics of egg yolk. *Food Hydrocoll*. 2020;100:105399. doi:10.1016/j.foodhyd.2019.105399.
19. Cheng Y, Liang K, Chen Y, *et al*. Effect of molecular structure changes during starch gelatinization on its rheological and 3D printing properties. *Food Hydrocoll*. 2023;137:108364. doi:10.1016/j.foodhyd.2022.108364.
20. Erturk MY, Le ANM, Kokini J. Advances in large amplitude oscillatory shear rheology of food materials. *Front Food Sci Technol*. 2023;3:1130165. doi:10.3389/frfst.2023.1130165.
21. Zhang Q, Chen Y, Zhou A, *et al*. An end-to-end AI framework for data-driven evaluation and optimisation of direct ink writing-based 3D printing [published online November 16, 2025]. *Virtual Phys Prototyp*. Published online 2025:e2584948. doi:10.1080/17452759.2025.2584948.
22. Latimer GW Jr, ed. *Official Methods of Analysis of AOAC International*. 20th ed. Rockville, MD: AOAC International; 2016. AOAC International.
23. Folch J, Lees M, Sloane Stanley GH. A simple method for the isolation and purification of total lipides from animal tissues. *J Biol Chem*. 1957;226(1):497-509. doi:10.1016/S0021-9258(18)64849-5.
24. Mshayisa VV, Van Wyk J, Zozo B. Nutritional, techno-functional and structural properties of black soldier fly (*Hermetia illucens*) larvae flours and protein concentrates. *Foods*. 2022;11(5):724. doi:10.3390/foods11050724.
25. International Organization for Standardization. *ISO 2591-1:1988: Test Sieving—Part 1:*Methods Using Test Sieves of Woven Wire Cloth and Perforated Metal Plate. Geneva, Switzerland: International Organization for Standardization; 1988. Accessed July 15, 2026. https://www.iso.org/standard/7569.html
26. Zhou P, Zhong K, Zhu Y. Numerical study of hydrodynamic cavitation pretreatment of food waste: Effect of pressure drop on the cavitation behavior. *Processes*. 2024;12(2):300. doi:10.3390/pr12020300.
27. Ewoldt RH, Hosoi AE, McKinley GH. New measures for characterizing nonlinear viscoelasticity in large amplitude oscillatory shear. *J Rheol*. 2008;52(6):1427-1458. doi:10.1122/1.2970095.
28. Joyner HS. Nonlinear (large-amplitude oscillatory shear) rheological properties and their impact on food processing and quality. *Annu Rev Food Sci Technol*. 2021;12(1):591-609. doi:10.1146/annurev-food-061220-100714.

29. Ewoldt RH, Winter P, Maxey J, McKinley GH. Large amplitude oscillatory shear of pseudoplastic and elastoviscoplastic materials. *Rheol Acta*. 2010;49(2):191-212. doi:10.1007/s00397-009-0403-7.
30. Kumar S, Queiroz LS, Marie R, *et al*. Gelling properties of black soldier fly (*Hermetia illucens*) larvae protein after ultrasound treatment. *Food Chem*. 2022;386:132826. doi:10.1016/j.foodchem.2022.132826.
31. Renzetti S, Henket J, Raaijmakers E, van den Hoek I, van der Sman R. Hydrogen bond density and glass-transition temperature govern gelatinization and gel rheology in cereal and tuber starches. *Curr Res Food Sci*. 2025;10:101101. doi:10.1016/j.crfs.2025.101101.
32. Nickerson MT, Paulson AT, Speers RA. Rheological properties of gellan solutions: Effect of calcium ions and temperature on pre-gel formation. *Food Hydrocoll*. 2003;17(5):577-583. doi:10.1016/S0268-005X(02)00075-9.
33. Klost M, Ramirez-Huerta MI, Drusch S. Heat-induced gelation of protein from mealworm (*Tenebrio molitor*): Influence of pH and zinc concentration. *Food Hydrocoll Health*. 2022;2:100105. doi:10.1016/j.fhfh.2022.100105.
34. Tavagnacco L, Chiessi E, Severini L, *et al*. Molecular origin of the two-step mechanism of gellan aggregation. *Sci Adv*. 2023;9(10):eadg4392. doi:10.1126/sciadv.adg4392.
35. Maldonado-Rosas R, Tejada-Ortigoza V, Cuan-Urquizo E, *et al*. Evaluation of rheology and printability of 3D printing nutritious food with complex formulations. *Addit Manuf*. 2022;58:103030. doi:10.1016/j.addma.2022.103030.
36. van der Sman R, Tian B, Ghoreishy SA, Noort M. Relationships between printability and rheology of inks for personalized nutrition. *Curr Res Food Sci*. 2025;11:101220. doi:10.1016/j.crfs.2025.101220.
37. Duvarci OC, Yazar G, Kokini JL. The comparison of LAOS behavior of structured food materials (suspensions, emulsions and elastic networks). *Trends Food Sci Technol*. 2017;60:2-11. doi:10.1016/j.tifs.2016.08.014.
38. Wang Y, Selomulya C. Food rheology applications of large amplitude oscillation shear (LAOS). *Trends Food Sci Technol*. 2022;127:221-244. doi:10.1016/j.tifs.2022.05.018.
39. Yazar G, Duvarci OC, Tavman S, Kokini JL. Effect of mixing on LAOS properties of hard wheat flour dough. *J Food Eng*. 2016;190:195-204. doi:10.1016/j.jfoodeng.2016.06.011.
40. Qin Z, Yang Y, Zhang Z, *et al*. A critical review: Gel-based edible inks for 3D food printing: Materials, rheology-geometry mapping, and control. *Gels*. 2025;11(10):780. doi:10.3390/gels11100780.
41. Outrequin TCR, Gamonpilas C, Sreearunothai P, Deepaisarn S, Siriwatwechakul W. Machine learning-assisted evaluation of filament spreading during extrusion-based 3D food printing: Impact of rheological and printing parameters. *J Food Eng*. 2024;381:112166. doi:10.1016/j.jfoodeng.2024.112166.
42. Tan C, Toh WY, Wong G, Li L. Extrusion-based 3D food printing: Materials and machines. *Int J Bioprint*. 2018;4(2):143. doi:10.18063/IJB.v4i2.143.